Chapter 3

An Array of Vacuum Photodiodes

Plasma radiation contains valuable information concerning internal plasma dynamics. In the Caltech experiments, spectrometer data measures plasma flows [42] and unexpectedly large densities [45, 46]. Soft x-ray and vacuum ultraviolet measurements yield ion and electron temperatures during spheromak merging [47], and, on tokamaks, provide information about confinement, MHD instabilities[30, 48, 49], impurity levels [48, 50], and the presence of energetic electrons [31, 32]. This chapter reports the development of an array of vacuum photodiodes for broadband extreme ultraviolet (EUV) measurements of the Caltech Solar Loop Experiment. The data from the array provides important information regarding radiative losses from the plasma as well as magnetic reconnection during loop merging, as will be discussed in Chapter 4.

The need for an array of vacuum photodiodes originates from limitations encountered with the x-ray photodiodes described in Sec. 2.2.3. The x-ray diodes revealed energetic radiation bursts that occur simultaneously with the formation of a central bright region during counter-helicity merging [20]. However, the x-ray diodes have a single line of sight and cannot determine from where in the plasma the bursts originate. Their signals also have significant shot-to-shot variation even though the experiment is very reproducible. To address these issues, a twelve-channel array of vacuum photodiodes has been built to provide spatially and well as temporally resolved radiation data. The array can detect variations in radiation along the plasma loops as well as variations of emission from the loop apex as the plasma expands outward.

Vacuum photodiodes are simple and cost-effective radiation diagnostics that respond primarily to EUV radiation [48, 50]. The EUV radiation band, defined below, is important for colder plasmas such as those produced by the Caltech Solar Loop Experiment because such plasmas tend to radiate away large quantities of heat via EUV line emission, as will be discussed in Chapter 4. Vacuum photodiodes operate on the photoelectric effect: sufficiently energetic photons strike a metal plate, called the cathode, and eject electrons that are then collected at the anode, as shown in Fig. 3.1. The resulting current is measured and gives an estimate of the incident photon flux. Vacuum photodiodes have an excellent time response due to the near-instantaneous nature of the photoelectric effect, allowing for sub-nanosecond time resolution [51, 52]. Their simplicity and compact size allow many detectors to be fielded on an experiment. Historically, vacuum photodiodes were extremely important during the 1970's and 1980's when conventional silicon x-ray diodes had a dead layer that prevented them from detecting UV radiation [49]. They were used for temperature studies of fast laser-produced plasmas [53], for impurity measurements on tokamaks that did not emit significantly in the soft x-ray regime [48], and for the study of edge-plasma phenomena such as plasma-wall interactions and H-mode phenomena [49]. In the early 1990's, International Radiation Detectors manufactured silicon photodiodes without a dead layer, and since then silicon diodes have been adopted as the standard for soft x-ray work [54]. However, vacuum photodiodes are still in use and are being considered for fusion-grade tokamaks such as ITER and JET where the radiation levels are too strong for non-metallic components [55, 56].

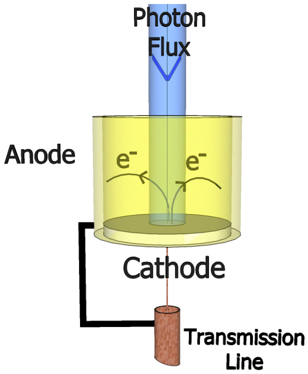

Figure 3.1: A vacuum photodiode consists of a cathode, in this case a metallic disk, that photoemits electrons when irradiated by EUV photons, depicted here by the blue incident column. The emitted electrons are then collected at the anode, a metallic cylinder coaxial with the cathode. The photocurrent from cathode to anode is measured and gives an estimate of the photon flux.

The range of sensitivity of bare (unfiltered) tungsten cathodes is quoted at 20 - 120 nm [48] and 5 - 120 nm [50], and this range is largely independent of the cathode metal, as will be discussed in Sec. 3.2.1. The photoyield for aluminum is shown in Fig. 3.2, and the peak response lies in the EUV wavelength range. For reference, the wavelengths and photon energies for various types of ultraviolet radiation are as follows: the UV range spans 100 - 400 nm (3.1 - 12.4 eV), vacuum ultraviolet (VUV) spans 10 - 200 nm (6.2 - 124 eV), and EUV spans the more restrictive range 10 - 121 nm (10.2 - 124 eV) [57]. Higher energy photons are typically classified as soft x-rays, although the exact distinction between EUV and x-ray seems to be a matter of opinion.

Vacuum photodiodes present an attractive means of studying bright spot formation on the Solar Experiment. Since the material cost of each individual detector is small, a large array can be constructed for a low cost, with the main expenditures coming from auxiliary equipment such as cables and mechanical support. Each detector is sufficiently fast to resolve the radiation bursts, and an array of such detectors will give the desired spatial resolution. This chapter details the design

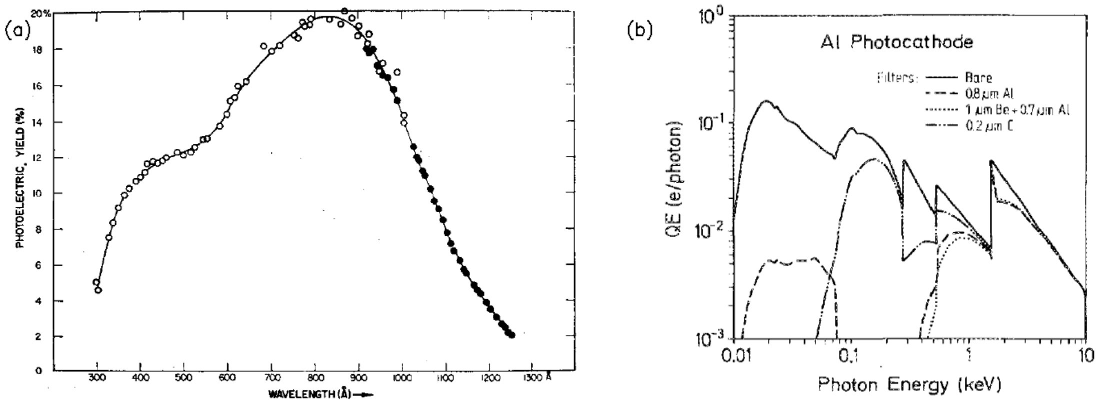

Figure 3.2: (a) The photoelectric yield of an aluminum cathode, plotted as a function of wavelength, reproduced from Ref. [58] (b) The yield of an aluminum cathode, as a function of energy, over a very broad range, reproduced from Ref. [49]. The peak in yield is in the EUV range. These yields will hold for an average aluminum cathode to within ±30% [59]

and construction of the array. Section 3.1 describes the experimental setup used to test vacuum photodiode prototypes. Section 3.2 discusses the photoelectric effect, cathode design, means for measuring the photocurrent, and the need for a bias voltage. Section 3.3 discusses various types of electrical interference along with measures taken to suppress them in the detector signals. In Sec. 3.4, the problem of the charged particle background is analyzed along with a magnetic shielding scheme. In Sec. 3.5, the physical layout of the array is discussed, and the collimation system used to isolate the field of view of each detector is described in detail.

3.1 Setup on the Test Chamber

Preliminary work with the photoelectric effect and vacuum photodiode prototypes was conducted on a small vacuum chamber, called the test chamber, where UV radiation was generated by a PerkinElmer short-arc xenon flashlamp [60] rather than by a plasma experiment. This provided a reproducible and reliable UV source without the electrical noise associated with the main experiment. The flashlamp pulse duration was roughly 10 μs, comparable to the lifetime of the Solar Loop Experiment. Also, the test chamber could be brought up to atmospheric pressure and opened in a matter of an hour, which allowed for more frequent testing and changing of detector design.

Fig. 3.3 shows the setup on the test chamber. Cathodes were mounted in a BNC feedthrough flange opposite to the flashlamp. The flashlamp, however, cannot simply face into the chamber through outside a window port because EUV radiation does not transmit efficiently through quartz windows[1]. To solve this problem, a mount was designed[2] to eliminate the need for a window by

---

[1] For various window transmission curves, see Ref. [61].

[2] The mount was designed by Shreekrishna Tripathi, whom the author graciously acknowledges for assistance in the early stages of this work.

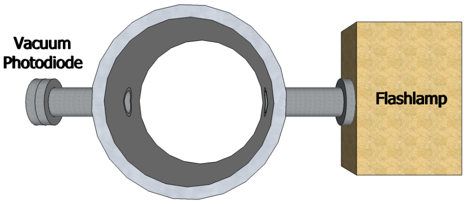

Figure 3.3: For preliminary testing of vacuum photodiodes, a xenon flashlamp was mounted directly on a small vacuum chamber to provide a reproducible source of EUV radiation.

Wavelength (nm)	Fraction of Output Power
100-150	.09
150-200	.10
200-250	.15
250-300	.10
300-400	.10
400-500	.14
500-600	.07
600-700	.05
700-800	.04
800-900	.07
900-1000	.05
1000-1100	.04

Table 3.1: The power distribution of the xenon flashlamp extends into the UV and EUV range. These numbers do not account for the attenuation introduced by the window of the flashlamp.

holding the flashlamp flush against the port on the test chamber. An o-ring between the lamp and port maintains vacuum. This setup guarantees maximal transmission of EUV light.

The flashlamp radiates from 1100 nm down to about 100 nm, so part of its spectrum is detectable by a vacuum photodiode. Table 3.1 shows the flashlamp power distribution as a function of wavelength, but the window of the flashlamp itself attenuates a portion of this radiation. For the window believed to be installed on the flashlamp, attenuation begins at 200 nm, and at wavelengths below 105 nm no radiation is transmitted. The exact transmission curve can be found in the flashlamp manual [60]. In spite of the window attenuation, sufficient EUV radiation was transmitted to produce a readable signal on the vacuum photodiodes.

3.2 Photoemission and Cathode Design

The photoelectric effect is usually discussed for photons at or near the work function of the emitting metal. The photoelectric effect induced by EUV photons, whose energies are several times the work function, is quite different and has implications for the design of a vacuum photodiode cathode. In this section, we review the photoelectric effect in the UV range, discuss options for cathode design, introduce schemes for measuring the photocurrent, and demonstrate the need for a bias voltage.

3.2.1 Review of the Photoelectric Effect in the UV

Photoelectric emission by UV photons is different from emission by visible light; the UV yields are 10 to 100 times higher and are more stable with respect to surface conditions. These effects can be explained by invoking a surface and volume effect. The following section reviews the early literature on the subject.

The photoelectric effect has a much greater yield in the UV range than from visible and near-UV photons, as was observed in the first measurements of the photoelectric yield in UV [62] and repeatedly in subsequent work. For Pt and Ta, the yields at wavelengths less than 100 nm are 10 to 100 times higher than for wavelengths 200 - 300 nm [63]. These high yields have important implications in various gas discharges such as glow discharges, sparks, and Geiger counters [64, 63]. For vacuum photodiodes, this increase in yield is a double blessing. First, the increased yield bolsters the signal-to-noise ratio, helping the signal stand out above the inevitable electrical noise. Second, the increase of yield in the UV makes the detector relatively insensitive to visible and near-UV light in comparison with EUV radiation.

UV photoemission is not as sensitive to surface conditions as emission in the visible and near ultraviolet, which is “extremely sensitive to the past history of the surface” and requires “careful outgassing procedures” [65]. The change in UV yield due to surface conditions is at most a factor of 10 instead of 50 to 500 for the visible [64]. No appreciable change in UV photoyield was found after exposure to air for 17 hours following heat treatment [63], and the yield has been repeatable upon multiple exposures to air [65]. Even more convincing, the response of a set of vacuum photodiodes was stable over several months of use in a tokamak [48, 50]. The yield is not completely independent of surface conditions; sand-blasting an aluminum surface drops the yield by a factor of two [58], and all previous workers have at the very least sanded the surface and cleaned it with solvents to remove gross surface contaminants. However, more extreme measures such as heat treatment, frequently used in work with the photoelectric effect induced by visible or near-UV light, are not needed for vacuum photodiodes, and their signals appear to suffer little long-term degradation.

Cairns and Samson measured the yields of relatively untreated metals and concluded that untreated photocathodes can be used with a probable uncertainty of about ±30% in the range 110 to 40 nm [59]. They focused on the reproducibility of the yield and tested “normally available samples” instead of specially prepared and ultra-pure samples. They stated that “different samples can be expected to have similar yields only if their surfaces are smooth and polished” but “a mirror-like finish, is, however, not essential.” Exposure to He, Ar, and Xe did not alter the yields nor did exposure to air at atmospheric pressure, and the yield of silver at 58.4 nm remained constant over 50 hours at 10^{-5} torr.

The different yields between the UV and visible ranges can be explained by proposing two types of photoelectric emission: a surface effect and volume effect. The surface effect denotes emission from the first several monolayers of the metal and is produced by photons just above the threshold frequency. In contrast, the volume effect is produced by UV photons that penetrate the surface of the metal and eject electrons from the bulk. Hinteregger proposed a theoretical model involving the volume effect to explain the rise in yield in the UV, the lower energy distribution of emitted electrons, the relative insensitivity to air exposure, and why increased temperature causes a decrease in emission [66]. It should be noted, however, that Cairns and Samson attribute the stability of the yield in the UV to the decrease in reflectance as opposed to the onset of a volume effect [59].

In summary, the photoelectric effect is easier to work with in the UV range than in the visible range. The yields are appreciably greater, which helps distinguish the signal from the inevitable electrical noise of plasma experiments. The yields are also not overly sensitive to surface conditions and are stable over long periods of time. These two features make vacuum photodiodes an attractive and low-maintenance diagnostic.

3.2.2 Cathode Material and Surface Conditioning

Cathode properties such as area, material, and surface condition all affect the amount of charge emitted during a shot and hence the size of the signal. Due to the large power levels of the Caltech experiment, the vacuum photodiode signals are quite large, so the cathodes do not need to be optimized for maximum signal size. Instead, the cathodes are designed for reproducibility, robustness, and simplicity, in the spirit of Ref. [59]. The cathodes in use on the array are aluminum disks that were lightly sanded, but other options were tested, as is discussed below.

The light sanding of the aluminum cathodes removes gross surface contaminants and improves the signal strength. Further surface conditioning can improve the signal levels even more but is not a robust technique. We have found that rigorously sanding the cathode surface to a shine boosts the signal by a factor of eight immediately afterwards, but this increase in yield gradually fades with time as a new oxide or surface layer slowly forms. Similar observations have been made by other researchers: even a laser-cleaned magnesium surface suffers an emissivity drop after only fifteen minutes *in vacuum* [67]! Thus, extreme surface conditioning may create a photoyield that slowly drifts with time. However, a light sanding improves the overall yield even in the long term and is a good practice provided that the sanded cathode is allowed some time in atmospheric conditions to equilibrate.

The choice of cathode material is not critical, as the yields for various metals are similar in the UV range to within a factor of unity [64, 59]. Our first choice of material was magnesium because of its low work function, but magnesium actually has an abnormally low yield in the UV [62]. Aluminum, on the other hand, has been used in previous photodiodes [49, 53] and is readily available. We tested the differences between aluminum and magnesium by placing a cathode of each material side-by-side on a conflat flange with two isolated electrical feedthroughs, allowing both cathodes to be tested simultaneously. Both disks were sanded to a shine and were then exposed to identical conditions (i.e., humidity, atmospheric pressure, vacuum). The yields, measured over the course of weeks, showed that aluminum emits more electrons than magnesium when irradiated by the flashlamp. The difference in yield diminished somewhat over time, but after several weeks the ratio of aluminum to magnesium yields settled to a value around three. Thus, aluminum was chosen for the final cathode material.

When used in the actual plasma experiment, the vacuum photodiode signals are quite large and do not require more emissive surfaces. Should there be a need for larger signal amplitudes, perhaps if a filter is being used, simply increasing the cathode area might be sufficient. Another trick would be to tilt the cathode, which can increase the yield due to a decrease in reflections [58].

3.2.3 Measuring the Photocurrent

Here, we discuss possible schemes for measuring the photocurrent, namely, with and without amplification. On the actual plasma experiment, the vacuum photodiode signals are large enough to be read directly without amplification, simplifying auxillary electronics and reducing potential sources of noise. However, amplification was needed for work on the test chamber where the signals were generated by the flashlamp. Amplification might also be required if filters are placed on the vacuum photodiodes.

The simplest scheme for measuring the photoelectric signal is to run the photocurrent $I(t)$ through a resistor R and to measure the voltage drop $V(t) = R \cdot I(t)$. For various reasons, R should be 50 Ω; this choice (i) avoids reflections in the signal line (ii) minimizes RC distortion due to stray capacitance, and (iii) is the built-in termination of the DAQ. These issues are discussed below. This scheme works well for large signals, such as those produced by the main chamber, but proves problematic for smaller signals, such as those produced by the flashlamp. Preliminary calculations for the flashlamp predict a photocurrent per unit cathode area of 10^{-5} A cm^{-2}; across a 50 Ω resistor, this gives signals in the range of $5 \cdot 10^{-4}$ V, which is at the limit of the DAQ's sensitivity.

Reflections in a cable occur when the termination of the cable differs from its characteristic impedance [68, ch. 2], which is typically 50 Ω. Reflections become problematic when the pulse duration is short and the cable is long. The cables used for the array are about ten meters long, and the speed of signals in this cable is approximately $c_c = 2 \cdot 10^8$ m/s, so reflections become an issue when the signal varies on a timescale faster than $\tau = 2 \cdot l/c_c = 100$ ns. Since the vacuum photodiodes are built to observe fast UV spikes, an impedance mismatch is unacceptable, and a 50 Ω termination is required.

RC distortion is an unwanted effect where stray capacitance in the cable and detector smears out the signal. The RC circuit is formed by the cable and vacuum photodiode capacitance together with the termination resistance, as shown in Fig. 3.4. We can work out the distortion by modeling the vacuum photodiode as a current source $I(t)$ and solving for the voltage across the resistor $V_R(t)$, which is the voltage measured by the DAQ. The photocurrent flows both into the resistor and capacitor: $I = I_R + I_C$. Since the capacitor charge is $Q(t) = \int_0^t I_c(t')dt'$ and $V_R = V_C$, we have

$$V_R = I_R R = \frac{1}{C}Q = \frac{1}{C}\int_0^t I_C(t')dt' = \frac{1}{C}\int_0^t (I(t') - I_R(t'))dt'. \tag{3.1}$$

Differentiating and rearranging,

$$I(t) = RC\frac{dI_R}{dt} + I_R. \tag{3.2}$$

This differential equation can be integrated after multiplying by the integrating factor $\exp(t/RC)$:

$$V_R(t) = RI_R(t) = \frac{1}{C}e^{-t/RC}\int_0^t e^{t'/RC}I(t')dt'. \tag{3.3}$$

This is the exact solution, and is not equal to the desired output $V_R = RI(t)$. However, we obtain $V_R \approx RI(t)$ when the time scale of the pulse is much greater than RC. One can see this by changing the integration variable of Eq. (3.3) to $\tau = t - t'$ and then assuming $I(t-\tau) \approx I(t)$. In the opposite limit where the pulse is much shorter than RC, the circuit acts like an integrator, $V_R(t) \approx \int I(t')/Cdt'$, and washes out the time resolution. Thus, compensating for low signal levels by using a larger termination resistance leads to signal distortion if the RC time approaches the signal duration. The effects of RC distortion can be avoided by keeping the termination resistance small. In fact, with R equal to the cable's characteristic impedance, there is absolutely no distortion, as the perfectly matched resistive load simply absorbs the signal with no reflection.

This model for RC distortion was verified on the test chamber by changing the length of cable used to carry the signal. The different lengths of cable had different capacitances that, combined with the 1 MΩ resistance of an oscilloscope, formed RC circuits with varying time constants. $V(t)$ was measured for each cable and found to be different even though the vacuum photodiode and flashlamp were unaltered. However, using $V(t)$ for each cable and inverting Eq. (3.3) for $I(t)$, the photocurrent trace for each cable was found to be more or less the same. That is, the differences in $V(t)$ came from cable distortion rather than an actual change in photosignal.

Signal amplification was required for work on the test chamber. One possible amplifier, shown in Fig. 3.5, is a modification of an inverting amplifier for use with a current source such as a vacuum photodiode. The input current flows across the top resistor so that the op-amp output voltage is IR. A small capacitor added across the resistor reduces ringing, although this slows the time response because it forms an RC circuit. For work on the test chamber, a 5 pF capacitor and a 50 kΩ potentiometer were selected to work with an AD711 op-amp; this circuit only slightly rounds a

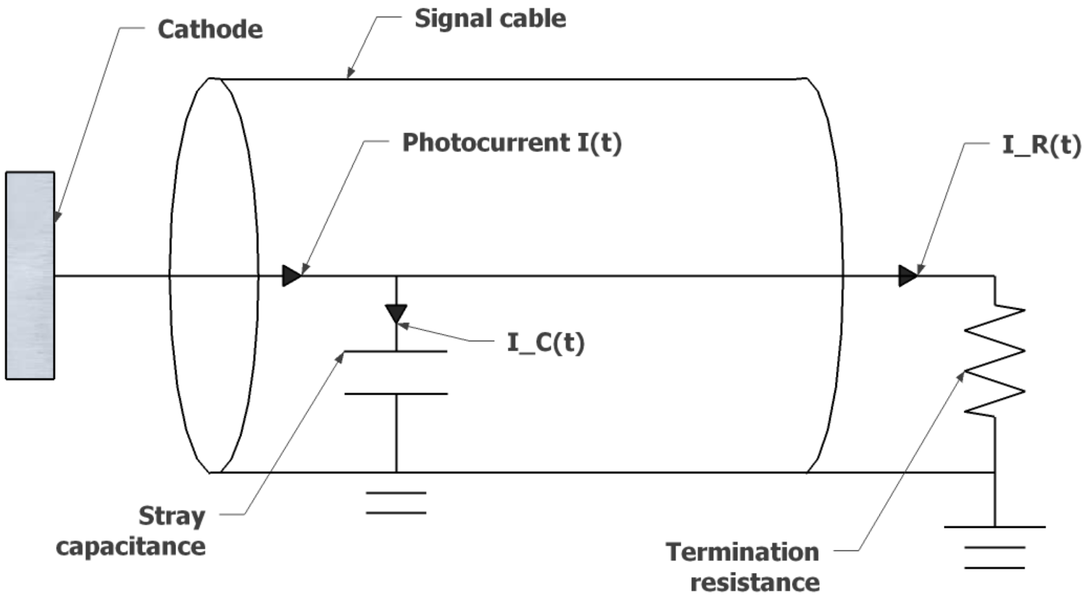

Figure 3.4: A circuit diagram showing the stray capacitance of the vacuum photodiode and cable. The stray capacitance combines with the termination resistance to form an *RC* circuit that distorts the photosignal.

10 μs square pulse. The signals on the main chamber are big enough to do away with the amplifier; quite the contrary, they actually require attenuation rather than amplification.

3.2.4 The Need for a Bias Voltage

A bias voltage between the cathode and anode is vital both for detector performance and troubleshooting. The bias helps overcome space-charge limitations, which inhibit full collection of the emitted charge. Also, changing the bias strength and polarity tests the vacuum photodiode for proper performance and helps identify the source of spurious signals. For these reasons, a significant amount of effort was invested in establishing a robust system for applying a bias voltage.

Space-charge limitation is an undesirable effect that takes place within a vacuum photodiode and can compromise the detector's accuracy. In a vacuum photodiode, electrons are emitted from the cathode and are collected on the anode, as shown in Fig. 3.1. However, an electron just above the cathode surface feels the negative potential of other recently emitted electrons on their flight to the anode; if this negative potential is sufficiently strong, the newly emitted electron might be reabsorbed by the cathode. This effect is known as space-charge limitation [69] and clearly is a potential source of error, as not every emitted electron is collected. Clearly, the larger the photocurrent, the larger the space-charge. However, the faster the electrons move from cathode to anode, the smaller the space-charge, and this last feature can be exploited to minimize the effects of space-charge.

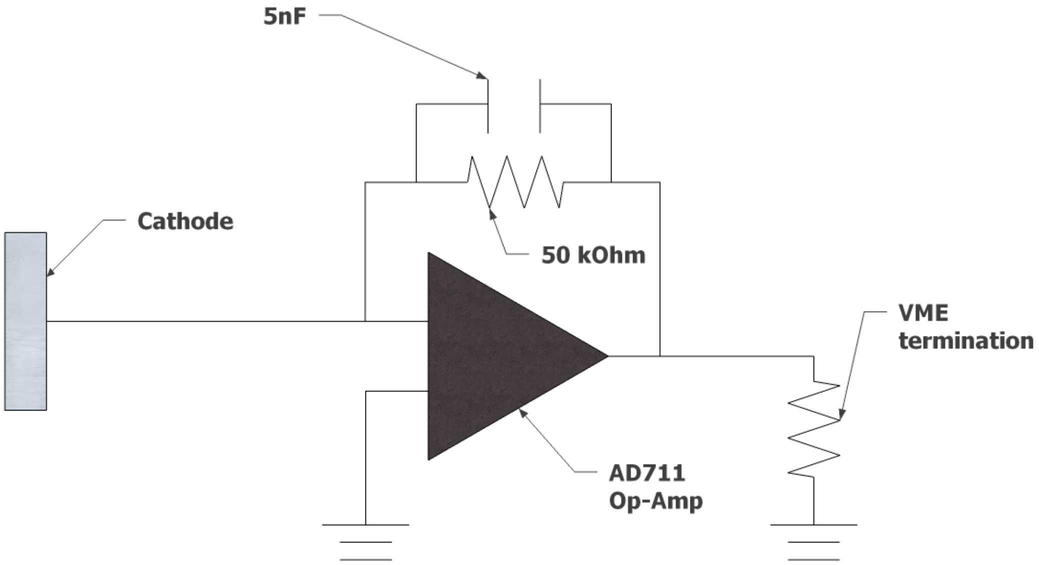

Figure 3.5: An amplifier for use with a vacuum photodiode. The op-amp converts the input current to an output voltage.

A proper bias lowers the cathode voltage relative to the anode so that the electric field rapidly moves emitted electrons from cathode to anode and lowers the negative charge density. With a large enough bias voltage, every electron that is emitted will be collected. In contrast, a reverse bias puts the cathode potential above the anode and inhibits the photocurrent to the point where no emitted electrons reach the anode. A reversed bias prevents accurate measurements but is useful for diagnosing the detector and also for estimating the energy distribution of the emitted electrons.

Space-charge effects are observed experimentally on both the test chamber and in the actual plasma experiment. The results of such an experiment performed on the test chamber are shown in Fig. 3.6. The horizontal axis is the applied bias voltage, which was varied with every shot. The vertical axis is the total *collected* charge, obtained by time-integrating the detector's signal. Three different cathodes are tested; each cathode has a different emissivity either through its total area, material, or surface conditioning, as discussed in Sec. 3.2.2. Thus, even though each cathode is exposed to the same level of radiation from the flashlamp, they emit different amounts of electrons. Fig. 3.6 shows several important features. First, the collected charge increases as the bias is made more negative, indicating that space-charge effects are limiting the collection of charge but can be overcome with a strong bias voltage. Second, as shown by cathode 1, the amount of collected charge plateaus as a function of bias voltage, indicating that every emitted electron can be collected.

However, by comparing cathode 1 to cathodes 2 and 3, the more charge emitted from a cathode, the stronger the bias voltage needed to reach the plateau, an observation consistent with space-charge limitation. On the main chamber, a bias of −66 V is used to guarantee accurate measurements; the difference between a −66 V bias and a typical −16 V bias is shown in Fig. 3.7. Returning to Fig. 3.6, with a reverse (positive) bias, the signal reversed polarity and became independent of the cathode! In this case, all electrons emitted from the cathode were reabsorbed due to the reversed bias voltage. These observed signals come from electrons emitted from the chamber wall and attracted to the cathode; the number of such electrons is obviously independent of the cathode.

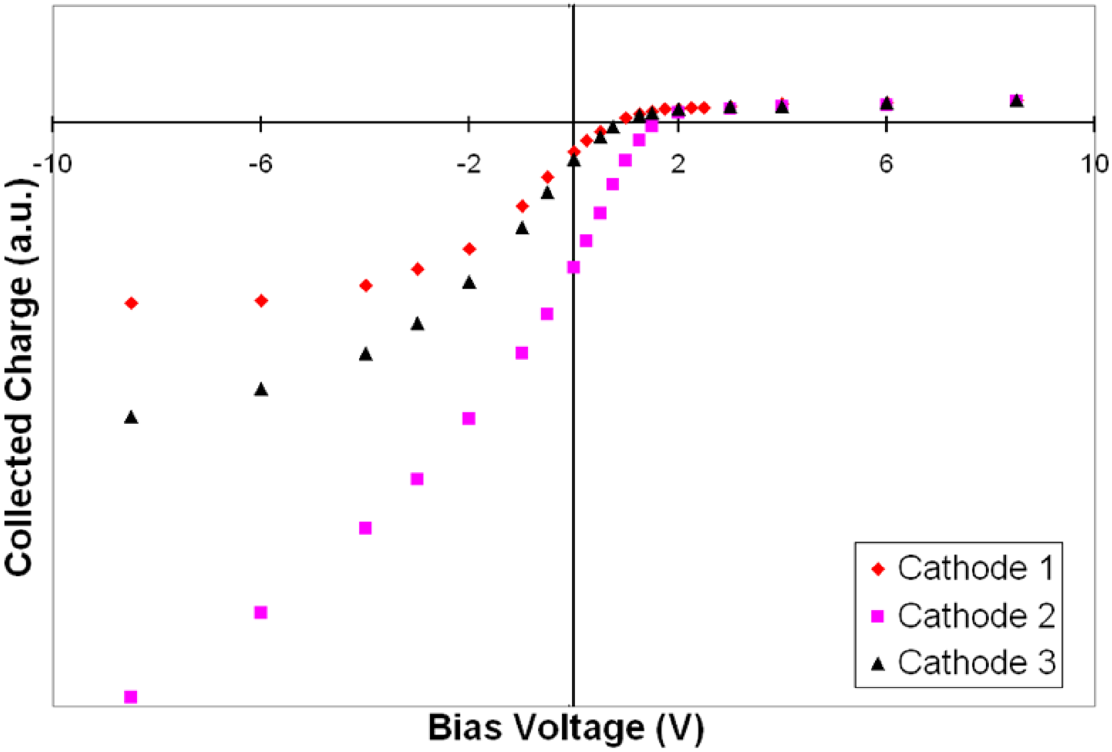

Figure 3.6: A sweep of the bias voltage reveals the effects of space-charge limitation on the amount of charge collected. Here, three different cathodes of varying emissivity were exposed to the flashlamp. Applying a more negative bias resulted in greater charge collection, indicating that the signals are space-charge limited.

A bias voltage is essential but must be carefully implemented. An ordinary voltage or battery placed directly into the signal line may carry unwanted stray capacitance and inductance. A solution proposed by Professor Paul Bellan places a capacitor in series with the detector as shown in Fig. 3.8. The capacitor is charged by a battery through large resistors; the RC time of the charging circuit greatly exceeds the shot length, so the photocurrent flows almost entirely through the capacitor. At the beginning of a shot, the capacitor is fully charged and holds the cathode potential below the anode potential. During the shot, the photocurrent discharges the capacitor, but if C is large enough

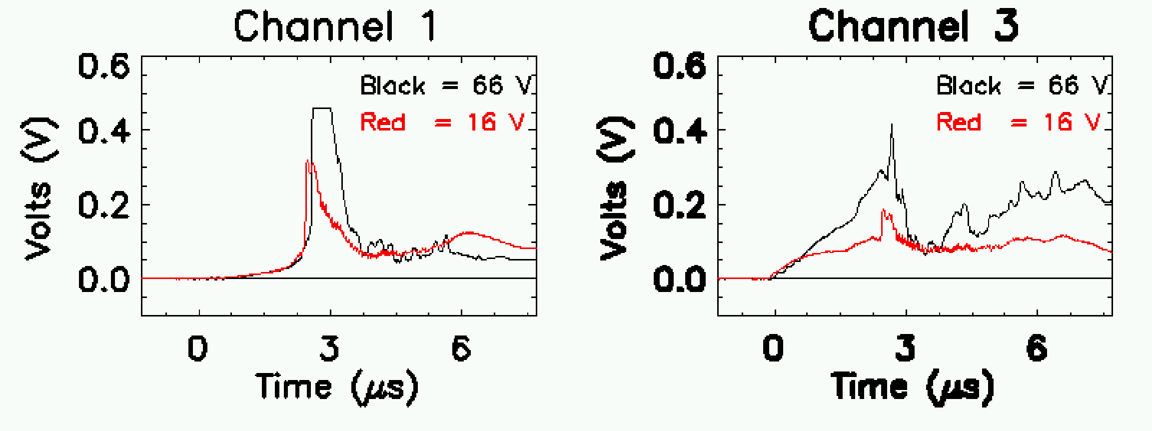

Figure 3.7: Vacuum photodiodes signals can be space-charge limited. Here, data obtained with different bias voltages are compared; vacuum photodiode channels 1 and 3 from the array are chosen as representative plots. The red traces are signals taken with a −16 V bias, and the black traces are taken with a −66 V bias. As shown, the larger bias voltage helps in the collection of photoemitted particles. The clipping seen in channel 1 is due to saturation of the DAQ and can be remedied by using attenuators.

then the bias voltage is more or less constant throughout the shot. In between shots, the battery slowly recharges the capacitor. For the array, $C = 100$ nF and $R = 470$ kΩ, giving $RC \sim .1$ s, which is much longer than the 10 μs duration of the plasma. The charge on the battery is $Q = CV$, so even a -10 V bias gives $Q = 10^{-6}$ C. In some of the most intense experiments performed at Caltech[3], the vacuum photodiode cathodes emit $Q \leq 1.1 \cdot 10^{-8}$ C; thus, the capacitors are not significantly drained over the course of a shot.

A non-trivial amount of work went into designing a circuit box to hold the bias circuits very close to the DAQ. The current design mounts directly to the boards on the DAQ so that no extra lengths of cable are needed in between the circuit box and the DAQ. This is done because, as discussed in Sec. 3.3.3, the use of braided coaxial cable introduces significant noise into the signal, and semi-rigid cables are rather expensive.

3.3 Noise Issues

In the author's opinion, no discussion of plasma diagnostics would be complete without some discussion of electromagnetic noise. As pointed out by Professor Bellan, the 59 μF capacitor in the main bank stores about one kilojoule of energy when charged up to 6 kV; this energy is released in a matter of 10 μs, giving power levels of 100 MW. Meanwhile, a diagnostic such as a vacuum photodiode produces signals on the order of 1 V across 50 Ω, which corresponds to 2 mW of power. Therefore, if even 0.00000001% of the power stored in the main bank couples to the vacuum photodiode, the

---

[3] Counter-helicity merging at a main discharge voltage of 6 kV and a gas supply voltage of 500 V. See, for instance, shots 7754, 7755, 7758, and 7759.

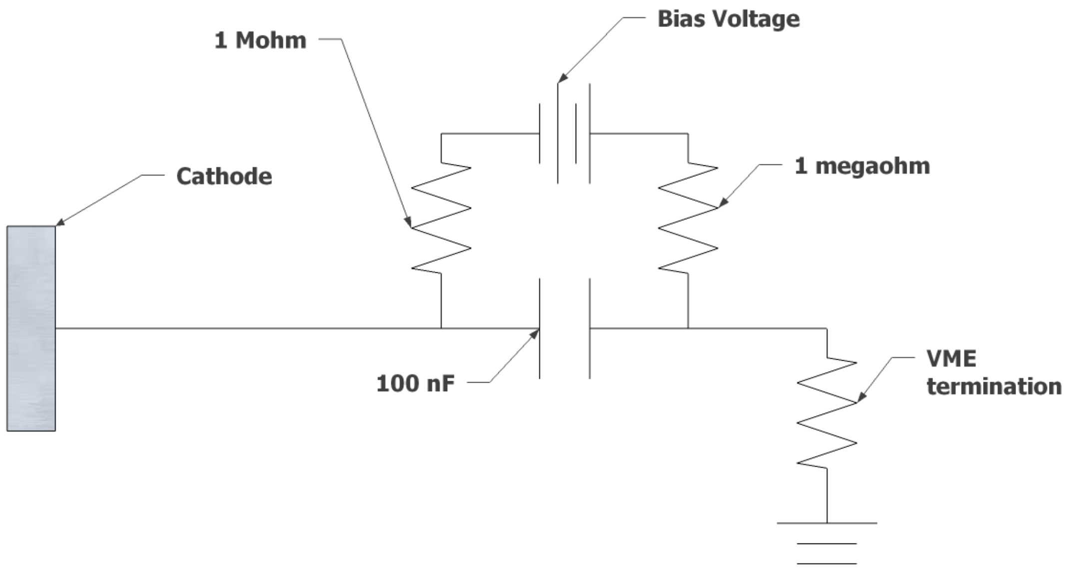

Figure 3.8: The circuit used to establish a bias voltage on the vacuum photodiodes. The signal is AC coupled to the DAQ through a 100 nF capacitor charged through large resistors. The RC time of the circuit greatly exceeds the shot duration, meaning the charging circuit is effectively isolated over the course of a shot.

desired signal will be overwhelmed.

Here, we discuss measures taken against electromagnetic noise, including the layout of the cathode and anode, use of an enclosure, use of semi-rigid coaxial cables, and dealing with radio-frequency (RF) ground loops. In some cases, several different changes were simultaneously implemented in a detector prototype to aggressively suppress the noise. Unfortunately, these simultaneous changes make it difficult to evaluate how well one particular noise-reduction technique worked independently of the others, and these instances are noted in the text.

3.3.1 Capacitive Coupling and Cathode-Anode Layout

Two types of electrical noise, capacitive and inductive pick-up, can plague plasma diagnostics and must be taken into consideration when designing the layout of the vacuum photodiode. Capacitive pick-up can be avoided by enclosing the detectors inside a metallic enclosure, or shield, and also by carefully laying out the anode and cathode. Inductive pick-up will be discussed in Sec. 3.3.2 and 3.3.5.

Capacitive coupling occurs between any two conductors as their relative voltage changes in time. Consider the “capacitor” formed by the detector cathode and one of the plasma electrodes. As shown in Fig. 3.9, if the electrode voltage is $V(t)$, then a charge $Q(t) = CV(t)$ is induced on the detector cathode, with C being the capacitance between the two conductors. As $V(t)$ varies in time, charge flows to and from the cathode and would be read as a photocurrent. Capacitive coupling can be eliminated by placing a third conductor, known as a shield or enclosure, between the first two. An enclosure from CompacRF serves as the shield; it encloses the detectors and intercepts the electric field lines between the detectors and the plasma electrodes. The enclosure makes direct electrical contact with the chamber wall, so enclosing the detectors essentially transfers the capacitive coupling between the plasma electrodes and detectors to coupling between the plasma electrodes and the enclosure. Of course, small holes are drilled through the enclosure to allow the detectors to see out into the plasma; these holes are further collimated as discussed in Sec. 3.5.3.

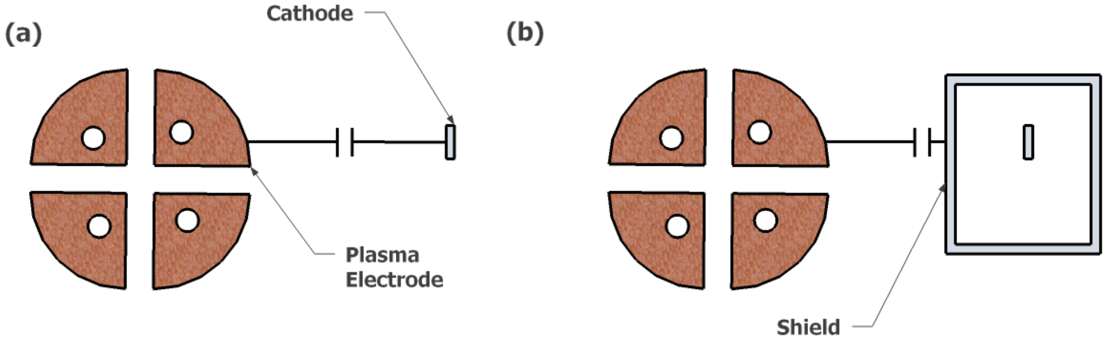

Figure 3.9: (a) Capacitive coupling between the detector cathode and the plasma electrode. (b) A shield placed between the two conductors stops the coupling.

It is suspected that further coupling to the detector cathode can exist even when the detector is housed inside the enclosure. In principle, one expects the enclosure to act as a Faraday shield and neutralize all interior fields. However, as will be discussed in Sec. 3.4.3, large interior electric fields still appear inside the enclosure because the enclosure does not fully enclose the detector; after all, the detector cables have to exit the enclosure through an aperture. Because of these large interior fields, further work must be done to reduce capacitive coupling between the enclosure and the cathode. The main idea is to shield the detector cathode as much as possible with the detector anode. This works because, while coupling to the cathode creates spurious signals, coupling to the anode is not detected because induced charge flows to the anode from ground rather than through the DAQ. The final layout, then, seeks to “enclose” the cathode as much as possible with the anode.

Early anode-cathode designs from detector prototypes provide examples of such coupling and proper shielding. In the first prototype, shown in Fig. 3.10.a, the cathodes were affixed with Torr Seal to the ends of long copper tubes that served as both anodes and collimators. These tubes were themselves glued with Torr Seal into holes drilled through the enclosure and protruded out. It was supposed that plasma hitting the anode/collimator would simply flow to ground without inducing a signal. However, the prototype was tested by firing the spheromak experiment, located at the opposite end of the vacuum chamber. No signal was initially registered, as expected, but after about 80 μs, as plasma from the spheromak finally reached the collimator/anodes, a signal was induced. This signal is believed to be caused by capacitive coupling between the anode and cathode[4]. Clearly, the anode should remain shielded inside the chassis, and the collimator should instead be an extension of the enclosure.

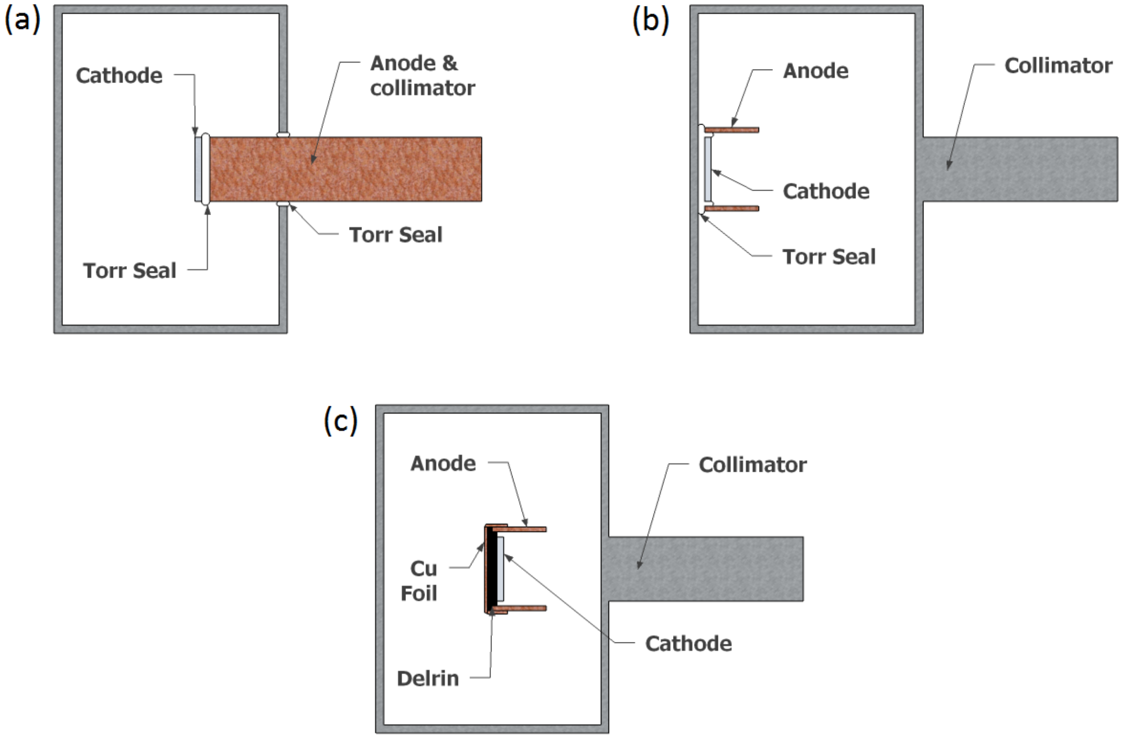

Figure 3.10: (a) The first cathode design used the anode as a collimator. This design does not keep the anode shielded, and it is suspected that anode-cathode coupling induced spurious signals. (b) Both anode and cathode are now shielded inside the detector, but the cathode was so close to the enclosure wall that strong enclosure-cathode coupling was suspected. (c) In the final design, the cathode is located in the middle of the enclosure and is surrounded, as much as possible, by the anode.

In another prototype, both anode and cathode were located inside the enclosure as shown in Fig. 3.10.b. The cathodes were affixed with Torr Seal to the far wall of the enclosure directly across the collimators. This design suffered from enclosure-to-cathode coupling rather than anode-to-cathode coupling, and the noise issues were not resolved in this prototype.

The final design further shielded the cathode from capacitive coupling by moving it away from the enclosure wall and surrounding it with the anode. The cathode was a circular aluminum disk, and the anode was a short length of copper tubing. The cathode was affixed to a delrin disk machined to fit inside the copper tubing, and a screw and nut were used to connect the cathode to the centerline

---

[4] The coupling could also be magnetic due to the current flowing from the anode to ground. Regardless, the conclusion is the same: the anode should be shielded inside the enclosure.

of the coaxial cable used to transmit the signal. Copper foil was wrapped around the back of the delrin holder and clamped to the cylindrical anode to shield the back of the cathode. The detector was suspended in the middle of the chassis by a planar piece of delrin so that the added spatial separation between the detector and the enclosure further reduced coupling. This layout eliminated much of the noise; however, other design modifications were simultaneously implemented. A high-quality enclosure was purchased from Compac RF to replace the thin aluminum chassis previously used, and electrical feedthroughs were eliminated by using semi-rigid coaxial cable to transmit the signal as discussed in Sec. 3.3.3. It is not certain which design modifications were most responsible for the improved signals.

3.3.2 Inductive Pick-Up and Ground Loops

Whereas capacitive pick-up is caused by time-varying electric fields, inductive pick-up results from time-changing magnetic fields. Should the conductors of a detector form a closed loop, then any change in the magnetic flux through that loop induces a voltage somewhere along the loop by Faraday's law. This voltage, or the currents associated with it, can couple to the signal and induce false readings. In particular, a closed loop may inadvertently be formed in the grounding of various instruments; this is called a ground loop and, although subtle, can easily distort the desired signal.

In many diagnostics, a ground loop can form along the outer conductor of the signal cable and the vacuum chamber as follows. The signal cables go to the DAQ where the outer conductor of the cable connects to the DAQ ground. The DAQ itself is grounded by a thick braided cable that connects to pipes in the ceiling, which is electrical ground for the building. The vacuum chamber is likewise electrically connected to building ground and hence to the DAQ ground. Therefore, the ground of a diagnostic is automatically connected to the chamber ground by virtue of being plugged into the DAQ. Now suppose that the diagnostic cable touches the chamber. This second connection forms a large ground loop spanning the laboratory, as shown in Fig. 3.11. Special care must be taken to electrically insulate the diagnostic from the chamber to avoid forming such loops.

Figure 3.11 shows the deleterious effects of a ground loop on a vacuum photodiode prototype. In the top plot, the uninsulated cable carrying the signal inadvertently made contact with a support rod in the ceiling. The resulting ground loop caused strange oscillations in the signal; in particular, the signal became negative, which is a clear indication of a spurious effect, as a vacuum photodiode signal is always positive. By simply moving the cable away from the ceiling rod, the ground loop was undone, and the signal returned to normal, as shown in the bottom plot[5]. As a second example of how ground loops can creep into the system, a small tear developed in the insulating sleeve of the signal line that allows contact between the signal cable and the chamber. The resulting ground loop

---

[5] Ironically, the ground loop suppresses the high-frequency noise, presumably by shunting some of the high-frequency ground currents. These ground currents will be discussed in Sec. 3.3.5.

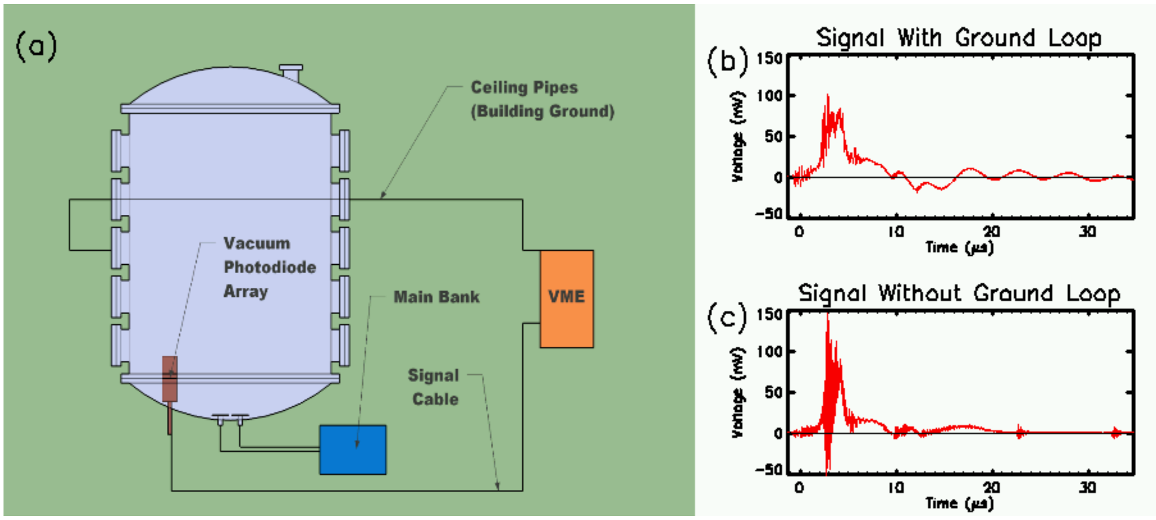

Figure 3.11: (a) Electrical contact between the vacuum photodiode array and the chamber will result in a ground loop extending back to the DAQ. (b) A vacuum photodiode signal taken with a ground loop in the system. Oscillations are observed, and the negative signal must be spurious, as the photosignal is strictly positive. (c) The signal with the ground loop removed.

induced a large spurious signal, but, worst of all, the contact between grounds was only maintained when the vacuum photodiode was rotated to face the plasma. When the detector was rotated away from the plasma, the contact pressure was released and the ground loop disappeared. This gave the ground loop signal the appearance of a plasma effect. When unusual signals such as the one in Fig. 3.11, appear, it is best to check for ground loops immediately.

3.3.3 Cables And Electrical Feedthroughs

Tests on a detector prototype showed that using semi-rigid coaxial cable (coax) to transmit the signal significantly reduces the noise levels. Semi-rigid coax has a solid and continuous outer conductor, in contrast with ordinary coax whose outer conductor is a braid of fine wires. Use of braided coax typically results in large noise levels at 1 - 2 MHz; semi-rigid coax not only reduces the noise amplitude but also results in noise of a higher-frequency, typically 3 - 5 MHz. The higher frequency noise is easier to distinguish from the actual photosignal. The solid outer conductor is a more effective shield [70] but is still flexible and easy to work with, although it is also significantly more expensive.

The use of semi-rigid coax presents a solution to a second problem: how to take the signal out of the vacuum chamber. Vacuum flanges with electrical feedthroughs are available, but either (i) force a non-coaxial geometry, making the signal more susceptible to noise, or (ii) only offer a small number of feedthroughs per flange. Non-coaxial feedthroughs are a prime suspect for the large noise seen on prototypes. Instead of using a feedthrough flange, we decided to run semi-rigid coax through holes drilled in a cylindrical piece of delrin fit inside a length of steel tubing as shown in Fig. 3.12. The tubing exits the chamber through a quick-disconnect flange. The cables hold vacuum within themselves, and Torr Seal was applied to the small space between the cables and the delrin and also between the delrin and the tubing. Within the tubing, a vacuum-compatible insulating jacket is sleeved over the cables to insulate them from the tubing. This scheme allows many cables to exit vacuum though a relatively small space while maintaining vacuum and electrical isolation. With the thirteen-channel array, only a single small leak was found that was quickly fixed with a second application of Torr Seal.

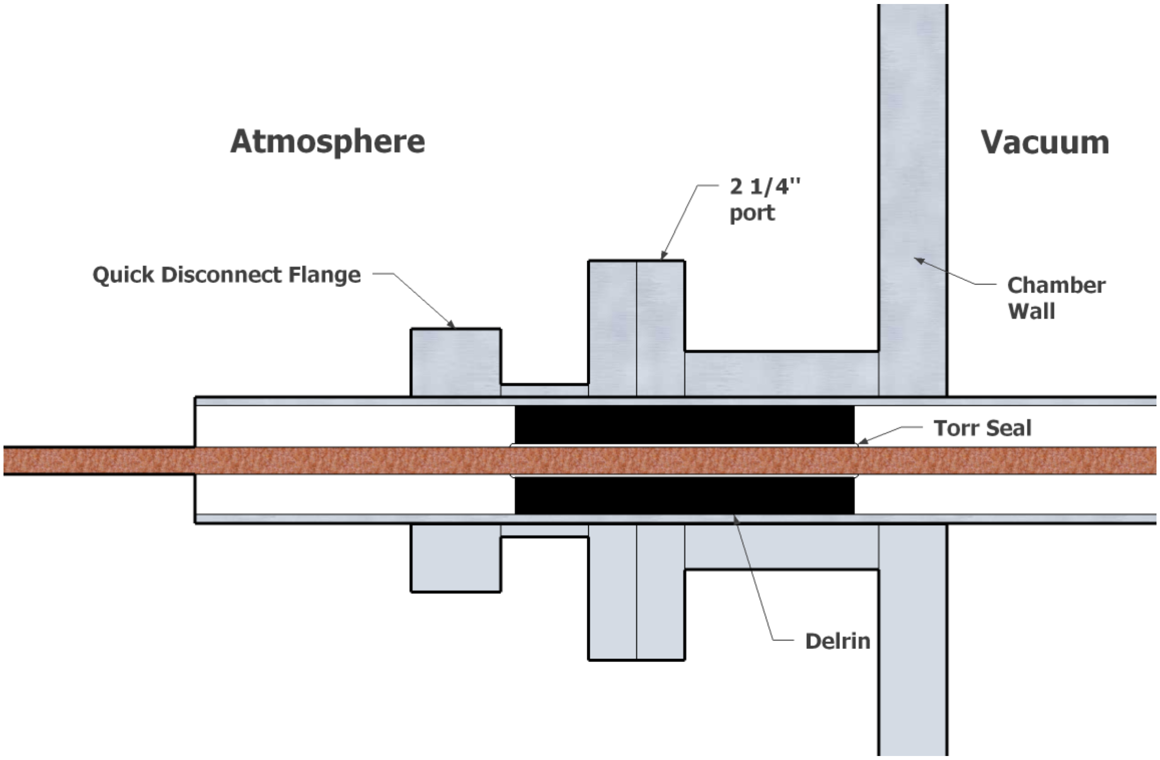

Figure 3.12: The semi-rigid cables exit the chamber through small holes drilled through a delrin piece. Only one cable is depicted in this figure, but this configuration allows the thirteen cables of the array to exit vacuum.

3.3.4 Blind Channel

When electrical noise appears on a diagnostic signal, it is difficult to determine whether the noise enters the signal in the detector itself or rather in the cables and electronics used to transmit the signal. A handle on the electrical noise is obtained by adding a blind channel to the array, as suggested by Professor Bellan. This channel is identical in construction to the other detectors, but there is no hole drilled in the enclosure to open the field of view of the blind channel to the plasma. Any signal read by the blind channel must be due to electromagnetic noise. The blind channel typically shows only high-frequency oscillations with zero mean value. If an unusual signal appears on the other channels but not the blind channel, then the signal must result from the vacuum photodiode being open to the plasma as opposed to noise.

3.3.5 RF Noise and Ground Currents

Despite the precautions described in this section, radio-frequency (RF) noise appeared in the vacuum photodiode signals, including the blind channel signal. As can be seen is Fig. 3.13, the noise amplitude was so that large that it obscured the desired photosignal. The problem was eventually ascribed to large RF currents flowing on the outer conductors of the signal cables. Ideally, such ground currents should not affect the actual photosignal propagating inside the cable, but small apertures in the bias circuit box allowed the RF ground currents to magnetically (inductively) couple to the photosignal. This coupling between signal and shield current is called surface transfer impedance [70] and can be difficult to identify. For instance, to test whether the bias circuit box was admitting noise, the signal cables were disconnected from it to isolate the noise admitted by the circuit box from noise admitted elsewhere in the circuit. However, no noise was detected because the RF ground currents were also disconnected. This test would have identified electrostatic (capacitive) coupling of noise through the circuit box apertures but failed to detect the *magnetic* coupling.

To eliminate the noise, the RF ground currents are diverted around the circuit boxes as follows. The outer conductor of each cable is shunted to the DAQ ground by attaching a clip between the cable and the DAQ frame. This shunt provides an alternate path for the RF ground current to flow. Ferrite cores placed around the cables downstream of the shunt increase the inductance of the path through the circuit box, and the ground current flows preferentially through the low impedance shunt. This strategy diverts almost all of the current and drastically eliminates the RF noise, as shown in Fig. 3.13.

The RF ground currents most likely result from an RF ground loop. Recall from Sec. 3.3.2 that a ground loop was avoided by insulating the signal cables from the chamber. As discussed in Sec. 3.3.3, this is achieved by sleeving the cables as they run through the support arm into the vacuum chamber. However, the cables are physically very close to the support arm, and there is a fair amount of capacitance between them. This capacitance can close the ground loop for RF currents because the capacitive impedance is very low and is effective a short as such high frequencies. The ground loop only exists for RF signals and hence is called an RF ground loop. The coupling could perhaps be reduced by shortening the length of the support arm or increasing its radius to reduce the capacitive coupling to the cables.

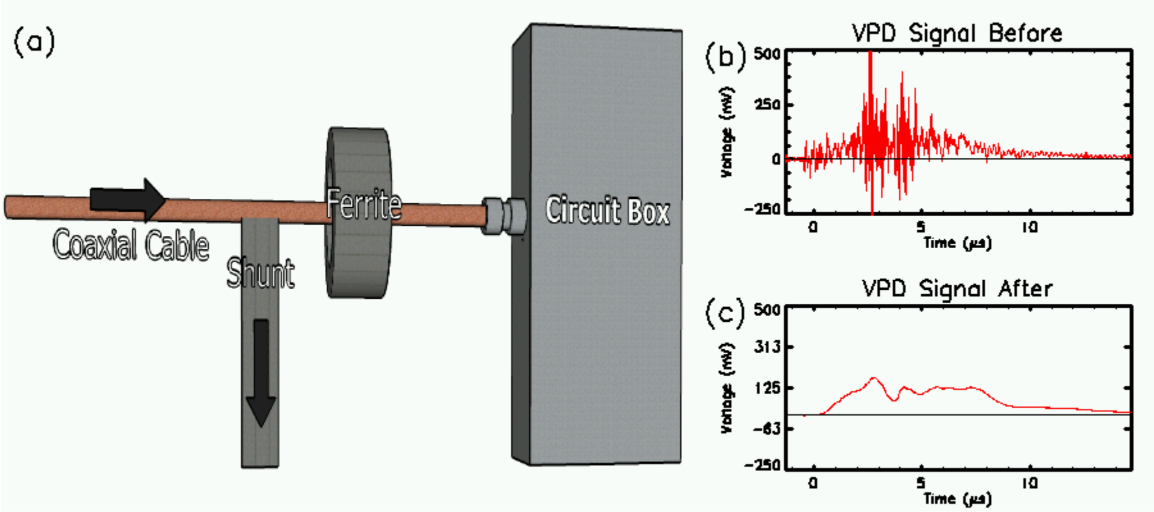

Figure 3.13: Large ground currents couple to the signal at the bias circuit box, introducing massive noise. By providing an alternate path for the current to flow and using ferrite cores to make the path through the circuit box high impedance, the large current are diverted from the circuit box, drastically reducing noise.

3.4 Charged Particle Background and Deflecting Magnets

Vacuum photodiodes work by the photoemission and collection of electrons. Unfortunately, plasma particles entering the detector can also be collected, in which case the detector output is no longer an accurate representation of the photon flux. These spurious effects can be avoided by placing a permanent magnet in front of the detector to deflect charged particle while allowing photons to pass. The effectiveness of such magnet in deflecting charged particles is discussed in Appendix B

The array was first built with a single neodymium magnet[6] placed on each collimator. These magnets were believed to be strong enough to deflect all charged particles, but spurious signals appeared on the array. These signals were not electromagnetic interference, because the blind channel did not register them. This section outlines the investigation into these signals, but the issues discussed are not necessarily unique to vacuum photodiodes and could be of use in a variety of instruments. Ultimately, the spurious signals were credited to a collusion of energetic ions passing the magnets and a large and unexpected electric field that appeared inside the array. All shots presented here were made with hydrogen gas in the counter-helicity configuration RL (see Sec. 2.1.3) with the charging voltage of the gas valve power supply voltage set to 500 V (see Sec.2.1.2).

3.4.1 Examples of Spurious Signals

A vacuum photodiode in proper operation should only output positive signals; that is, the only flow of charge should be electrons photoemitted from the cathode and collected at the anode. However,

---

[6] McMaster-Carr, part number 5902K61

the array occasionally produced negative signals, usually in very brief bursts but sometimes for more extended periods of time. The array also produced exceedingly large positive bumps at late times when no special optical activity was observed; these signals were also believed to be spurious. Specific examples of these two types of spurious signals are shown in Fig. 3.14. Note that the array has twelve channels, but often a single channel is plotted. The single channel shown is not necessarily representative of the entire array, as there is plenty of variation within the different channels in a single shot.

Fig. 3.14.a shows the trace from channel 5 of shot 6952; it has two negative spikes around 3.7 μs. These spikes must be spurious, as the photoelectric effect only produces positive signals. Channel 3 of shot 6953 has a large positive bump that occurs around 6.7 μs, as shown in Fig. 3.14.b. At this time, the Imacon images look dimmer than at earlier times in the shot, so this late peak is suspicious. The clipping seen here is saturation of the DAQ and is resolved by placing attenuators on the signal output. Fig. 3.14.c shows data from channel 4 of shot 6960; it contains a negative spike preceding the large positive peak; this has been observed on other shots as well. Fig. 3.14.d shows another late positive peak, this time from channel 5 of shot 7064, but these data are obtained with no bias voltage applied to the detector. Without the bias voltage, the photosignal is suppressed, leaving the late positive peak in isolation.

3.4.2 Investigating the Spurious Signals

Adjustments of the array's bias voltage influenced the amplitude of the negative signals, suggesting that charged particles were responsible. The bias voltage was adjustable within from 0 to -16 V, and shots taken with half strength or no bias voltage produced larger and more frequent negative signals. This not only implied charged particles as the source of the negative signals but also suggested that these charged particles had energies on the order of 16 eV. Increasing the bias voltage to -66 V eliminated almost all negative signals apart from rare and very brief spikes. Secondary electrons are typically defined as electrons with energies less than 50 eV [71], so the fact that a -66 V bias eliminated the negative signals implies secondary electrons. The increased bias did not eliminate the late positive peaks. Also of note, the negative signals were disproportionately worse at discharges of 6 kV and 5 kV than at 4 kV.

The appearance of the negative signals was puzzling. The most likely explanation was that energetic electrons were passing the magnets and striking the cathode. However, Stormer analysis, discussed in Appendix B, suggested that an electron must have very high velocities, over 10^7 m/s or 300 eV, to pass the magnets. This scenario was rather unlikely. First, we did not anticipate such energetic electrons and certainly not in such large quantities. Second, altering the bias voltage, which was of the order of 16 V, influences the level of negative signal. 300 eV electrons would not have been affected by such a relatively small bias.

However, Stormer analysis suggested that moderately energetic ions could pass the magnet. Ions striking the cathode would produce a positive signal, explaining the large positive bumps. Ions could induce the negative signals as well through secondary electron emission such as Auger ejection, where an ion absorbs an electron from a nearby metallic surface and simultaneously liberates a second electron [72, 73]. However, there was a problem with this explanation. For ion energies below 1 keV, kinetic ejection of secondary electrons is improbable [73]. The primary means of secondary production is Auger ejection, meaning the secondary electrons must have an energy that is at most equal to the ionization potential of the ion minus two times the work function of the metal. For hydrogen, this maximum energy is 13.6 eV minus twice the work function, which is typically on the order of 3 or 4 eV. Since the bias voltage keeps the cathode at roughly 16 V below the anode, how could such electrons overcome the -16 V bias voltage to reach the cathode?

For completeness of discussion, there are other mechanisms for producing electrons inside the detector. UV radiation might photoemit electrons from the collimator wall, but this effect is expected to be negligible due to the small solid angle of the collimator as seen by the plasma. UV radiation could photoionize neutral gas inside the chassis, but the number of neutrals inside the array should be negligible. Neutral particles might also pass the magnet unaltered and create secondary electrons, although, at particle energies around 10 eV, this is practically ignorable [48].

3.4.3 Transient Voltages

The negative signals were finally explained when a potential difference between the vacuum photodiodes and the array enclosure was hypothesized and then measured. The voltage, plotted in Fig. 3.16, could reach over 600 V and reversed polarity around 5.7 μs. The origin of this voltage will be discussed below. When this voltage was positive, it provided a mechanism whereby secondary electrons could become sufficiently energetic to strike the cathode as follows. Energetic ions passed the magnets and entered the array; the transient voltage then repelled the ions away from the detector towards the enclosure wall, as shown by the red line in Fig. 3.15. At the wall, secondary electrons were ejected and then accelerated by the induced voltage towards the detector. Energized to hundreds of electron volts, the electrons were energetic enough to overpower the bias voltage and strike the cathode. However, this is not the complete story since a -66 V bias stopped all electrons from reaching the cathode. Since the anode was closer to the enclosure wall than the cathode, the electric field lines probably ended on the anode. Electrons likely struck the anode and produced more secondaries[7] [74]. These secondaries, if sufficiently energetic, could strike the cathode, as shown by the green lines in Fig. 3.15.

The late times of the positive peaks can likewise be explained due to the reversal of the induced

---

[7] Kinetic ejection of secondary electrons from primary electrons seems much more probable than kinetic ejection from primary ions. This is probably due to the inefficient energy transfer of ion-electron collisions [2, pg. 16].

voltage around 5.7 μs. After this time, ions were attracted towards the detectors. Above, we argued that the electric field lines end on the anode, but the ions must have collided with the cathode to produce a positive signal. Since ions are far more massive than electrons, it is conceivable that ions acquire enough forward momentum to reach the cathode directly, as suggested in Fig. 3.15, even if the field lines mostly end on the anode. Also, if the ions strike the anode, they might bounce and reach the cathode.

The origin of this transient voltage lies in the fact that the array has two "grounds:" the "detector" ground consisting of the anode and outer conductor of the signal cables, and the "chamber" ground consisting of the chamber and enclosure, as discussed in Sec. 3.3.1. Because the two grounds are kept electrically isolated in the vicinity of the chamber and because of the large distance of cable connecting them, a transient potential can develop between them. The potential difference might be due to inductive pick-up; consider the loop that follows the signal cable to the DAQ and then travels back to the chamber along building ground and finally jumps across the gap to join its starting point on the signal cable; see Fig. 3.11. This loop encloses a rather large area that is in the vicinity of the main capacitor bank. By Faraday's law, if the magnetic flux through the loop changes in time, then the line integral of the electric field must not vanish. However, most of the loop lies along conducting metal, so the electric field must, by and large, lie across the gap between the detector and the enclosure.

Finally, we note that the induced voltage is disproportionately smaller at low discharge voltages (3 and 4 kV) than at 5 kV or 6 kV. Fig 3.16 compares the voltage for 4 kV and 6 kV discharges. At 6 kV, the voltage reaches almost 700 V. At 4 kV, however, the voltage has at peak oscillation only 200 V, and the mean voltage is roughly 30 V. The amplitude of the transient voltage is thus non-linear in the discharge voltage. This explains why 6kV discharge voltage produced disproportionately more negative signals than 4kV. Also, in studying the difference between co- and counter-helicity merging [20], the amount of soft x-rays emitted likewise has a non-linear dependence on the discharge voltage. The two observations are perhaps related.

3.4.4 Upgrading the Magnets

Both types of observed spurious signals, negative dips and late positive peaks, are believed to be caused by ions entering the chassis and causing secondary electron emission. It is a rather bizarre conclusion that *positive* charge entering the array can ultimately lead to a spurious signal due to *negative* charge hitting the cathode. The large potential difference between the detector and the chassis, however, provides a mechanism for this phenomenon.

An obvious solution to these spurious signals, then, is to upgrade the magnets guarding the collimator entrance to deflect ions more effectively. As discussed in Appendix B, the deflecting power of a magnet is determined both by the field strength and also the spatial extent of this field.

To improve deflection, a new set of ultra-strong neodymium magnets was ordered, and the geometry of the magnets was changed. Two magnets are now used on each collimator and are seated in notches cut into the collimator to form a high-field gap region, as shown in Fig 3.17. In the original single magnet setup, the field strength decays rapidly with distance from the magnet, but in the new geometry the field is uniformly large within gap. The magnet upgrade successfully eliminates spurious signals. The field strength around the gap has been measured, so, if spurious signals do arise, the energies of the energetic ions passing the magnet can be estimated; see Appendix B.

3.5 Physical Layout and Geometry

This section focuses on the physical layout of the array, including its positioning in the vacuum chamber, its support system, and collimation. The array is situated to look across the electrodes, as shown in Fig. 2.1. In total, the array has thirteen channels, but one of them is the blind channel described in Sec. 3.3.4. The twelve active channels are arranged in a T-shape with seven channels in the vertical direction and six in the horizontal. This allows variations in the emission of the loop apex to be observed as the plasma expands outward and asymmetries between the top and bottom halves to be identified. The number of channels was limited by several factors. The method of taking the signal cables out of the chamber, described in Sec. 3.3.3, cannot support many more than thirteen cables; this limitation is actually set more by the size of the BNC connectors on the cable ends rather than by the radius of the cables themselves. Also, many of the DAQ channels are occupied by other diagnostics, and making more vacuum photodiode channels would require other diagnostics to be disconnected.

3.5.1 Array Positioning

Vacuum photodiodes need to be placed *inside* the vacuum chamber, in contrast to optical spectrometers and photodiodes that can leisurely measure plasma radiation through window ports. There are two reasons for this. First, EUV radiation suffers extreme attenuation through the vacuum windows used on the vacuum chambers [36, pg. 104]. Even MgF_2 windows, which will transmit UV, cut off photons of wavelength less than 150 nm [61]. Second, experiments on the test chamber indicate that vacuum photodiode signals fall off as the vacuum chamber pressure increases, and previous work on photocathodes also showed that pressures less than 10^{-4} torr are required [59]. For these reasons, the detector itself must be located inside the vacuum chamber. This requires that all material used to construct the detector must be vacuum compatible and that the signal cables must be taken out of the chamber, as discussed in Sec. 3.3.3. Moreover, the available ports on the chamber are not always aligned with the preferred line of sight, forcing the experimentalist to design a support system to hold the array in place, as discussed in Sec. 3.5.2.

The array currently looks across the electrodes as shown in Fig. 3.18; this positioning is chosen not only to view a profile of the plasma loops but also to avoid viewing arcing that occurs at the electrodes. Such arcing is suppressed early in the shot because of the design of the plasma electrodes, as discussed in Sec. 2.1.4. However, later in a shot, arcing is observed between and behind the electrodes, and such arcing produces radiation that vacuum photodiodes can detect. Since this radiation is not from the plasma itself, the detectors must be strategically placed to view the plasma but not the electrodes. The need for such strategic placement was made clear by a vacuum photodiode prototype placed on an angle port directly facing the plasma electrodes. The prototype's signal extended well past the lifetime of the plasma and looked like a rectified version of the current trace, as shown in Fig. 3.19; this signal was produced by arcing roughly in proportion to the absolute value of the current. The Imacon images in Fig. 3.19 confirmed that the interelectrode arcing dimmed at precisely the zeros of the current trace. To avoid picking up this signal, the array now looks across the electrodes with its vertical channels located 10.6 cm above the electrodes. Note that the x-ray diode head is pointed directly at the electrodes, so a portion of their signals might be from arcing rather than from the plasma.

3.5.2 Support System

The array is rather heavy and needs to be suspended in the chamber to look across the electrodes. The resulting torque on the support arm is significant, and a support system was implemented[8] to provide the mechanical strength needed to hold the array in place. The support arm for the array is 1" diameter stainless steel tubing, which runs through a 1" quick-disconnect flange. To add mechanical support, an aluminum bushing was machined and is held in place by two aluminum brackets, as shown in Fig. 3.20. The bushing keeps the support arm from bending too much under the torque, especially during installation and rotation. Two set screws in the bushing hold the tubing in place when tightened down.

3.5.3 Collimation

Each vacuum photodiode in the array should view a different area of the plasma. To prevent the fields of view from overlapping, collimating tubes are placed in front of each detector. The length and diameter of the collimator are chosen to maximize the area viewed while keeping each field of view separate. Here, we calculate the area viewed by each detector as well as an effective area that accounts for the shadow of the collimator; at the electrodes, each detector views an area of 69.3 cm^2 but an effective area of only 2.6 cm^2.

---

[8] Similar supports have been designed by Carlos Romero and Dave Felt for use with magnetic probe arrays. The author also acknowledges Joe Haggerty, Ali Kiani, and Brad St. John of the GALCIT shop for suggesting design improvements and for machining various components for this system.

Given a collimator of radius R and length L, we can calculate the detector's view cone, shown in Fig. 3.21. If we assume that the distance from the middle of the collimator to the plasma is D, then, at the plasma, the detector's view cone has a radius r_0 given by

$$r_0 = D\frac{2R}{L}. \tag{3.4}$$

The collimators have an inner radius of 0.38 cm and a length of 5.5 cm. The distance from the center of the electrodes to the middle of the array is 42 cm, and the distance from the center of the array to the center of the collimator is 7.8 cm, giving $D = 34$ cm. We then have $r_0 = 4.7$ cm. In an array, if the fields of view of each detector are not to overlap, then each detector should be separated a distance $2r_0$ from its neighbors. The collimator dimensions were chosen so that the twelve active detectors could cover most of the plasma without overlapping. Fig. 3.22 shows a picture of the electrodes along with the central axes of the vacuum photodiodes, showing the vacuum photodiode spacing relative to the electrode size. Also plotted in Fig. 3.22 is the effective viewing area of each vacuum photodiode, which will be computed below.

Although the detector's field of view is calculated as above, not all points within this field of view illuminate the detector equally. Plasma at the edge of the field of view weakly illuminates the detector because the collimator casts a shadow over the detector, as shown in Fig. 3.23. The detector thus responds differently to plasma at the edge of its field of view than to plasma at the center of its field of view. This is important when using the vacuum photodiode signals to estimate the radiation power density of the plasma. Our goal is to compute an effective viewing area that accurately reflects the amount of radiation a collimated detector sees given the shadowing effects of the collimator. This statement will be made precise by first considering the response of a non-collimated detector to a uniformly emitting source.

For a detector without collimation, it is straightforward to estimate how the detector will respond to an emitting source. First, let a point source emitting power P isotropically be given with a distance ρ to the detector and with angle α between the detector's normal vector and the line connecting the detector and point source. If the detector has area A_d with $A_d \ll 4\pi\rho^2$, the power P_d intercepted by the detector is

$$P_d(\rho, \alpha) = P\frac{A_d \cos\alpha}{4\pi\rho^2}. \tag{3.5}$$

The fraction in Eq. (3.5) is the ratio of the detector area presented to the point source divided by the surface area of a sphere of radius ρ. For a distributed source, one computes the detector response by integrating Eq. (3.5) over the distribution:

$$P_d = \int d\left(P_d(\rho, \alpha)\right) = \int \frac{A_d \cos\alpha}{4\pi\rho^2} dP. \tag{3.6}$$

In practice, the source is usually located far enough away from the detector that the variations in ρ and α are small, and both ρ and α are held fixed at some representative values. We also assume that the source is essentially planar and radiates homogenously with some power per unit area σ, so $dP = \sigma dA_e$, with dA_e being a differential surface element of emitting plasma. The detector response is then estimated using Eq. (3.5) with Eq. (3.6):

$$P_d = \frac{A_d \cos\alpha}{4\pi\rho^2}\sigma \int dA = \frac{A_d A_e}{4\pi\rho^2}\sigma\cos\alpha, \tag{3.7}$$

where A_e is the area of emitting plasma. For this discussion, the key quantity is the product $A_d A_e$, the detector area times the emitter area, as the detector response is proportional to this value assuming constant σ, ρ and α.

For a collimated detector, A_d, the area of the detector presented to the emitter, changes at different points in the emitter. Again, Fig. 3.23.a shows that only a fraction of the detector is illuminated by a point source not centered on the collimator axis. Equation 3.7 would then be

$$P_d = \frac{\int A_d(\mathbf{r}) dA_e}{4\pi\rho^2}\sigma\cos\alpha, \tag{3.8}$$

where $A_d(\mathbf{r})$ represents the detector area presented to a point source located at $\mathbf{r}$. Our task is to first compute $A_d(\mathbf{r})$ as a function of position. Second, we would like to define an effective emitter area A_e^* such that

$$A_d A_e^* = \int A_d(\mathbf{r}) dA_e. \tag{3.9}$$

A_e^* would be the area of an uncollimated detector that would have the same response to the uniformly emitting source as the collimated detector. A_e^* will be used to estimate the power radiated per unit area, σ, from the power incident on the detector:

$$\sigma = \frac{4\pi\rho^2 P_d}{A_d A_e^* \cos\alpha}. \tag{3.10}$$

We begin by determining the detector area presented to different points of the emitting plane. We first need to coin names for the different parts of the collimator. The collimator is sketched in Fig. 3.23.b, where we have labeled the top circle and bottom circle. We are interested in the illumination of the cathode, but this is equivalent to the illumination of the bottom circle. We then place our origin at the center of the bottom circle. Let a point source be located at a height z and at a cylindrical radius r. Because of cylindrical symmetry, we orient a Cartesian coordinate system such that the point source is located at the coordinates $(r, 0, z)$. The boundary of the shadow cast by the collimator is determined by drawing lines from the point source to the various points on the top circle; we then follow each line until it intersects the $z = 0$ plane. We call this procedure projecting, and our first step is to work out the equations of projection.

We first project a point (a, b, c) onto the $z = 0$ plane. We call the x and y coordinates of the projection x_p and y_p respectively; these points are drawn in Fig. 3.23.c. The vector joining the point $(r, 0, z)$ to (a, b, c) is parallel to the vector joining (a, b, c) to $(x_p, y_p, 0)$. Therefore, these vectors must be proportional to one another with a constant of proportionality λ:

$$(r, 0, z) - (a, b, c) = \lambda\left[(a, b, c) - (x_p, y_p, 0)\right] \tag{3.11}$$

Using the z component of this equation, we get $z - c = \lambda c$ or $\lambda = (z - c)/c$. We can now use λ to solve for x_p and y_p. The x and y components of Eq. (3.11) are

$$\begin{aligned} r - a &= \lambda(a - x_p) & (3.12) \\ -b &= \lambda(b - y_p) & (3.13) \end{aligned}$$

Solving for x_p and y_p gives

$$\begin{aligned} x_p &= \frac{az}{z-c} - r\frac{c}{z-c} & (3.14) \\ y_p &= \frac{bz}{z-c}. & (3.15) \end{aligned}$$

Using Eq. (3.14) and (3.15), we can project the entire front circle. We parameterize the front circle by the angle θ so that the circle is the collection of points $(R\cos\theta, R\sin\theta, L)$. The projection of each point is

$$\begin{aligned} x_p(\theta) &= \frac{z}{z-L}R\cos\theta - r\frac{L}{z-L} & (3.16) \\ y_p(\theta) &= \frac{z}{z-L}R\sin\theta. & (3.17) \end{aligned}$$

This projection is itself a circle of radius $Rz/(z - L)$ centered at $x = rL/(z - L)$, as shown in Fig. 3.23.d. The illuminated area of the bottom circle, then, is the intersection of the bottom circle with this projected circle. This area, denoted by $A_d(r, z)$, is computed numerically once the collimator dimensions R and L have been specified.

We can now use $A_d(r, z)$ in Eq. (3.8). We assume again that the distance ρ and angle α can be held fixed. The integral,

$$\int A_d(r, z)dA_e = \int_0^{r_0} A_d(r, z)2\pi r dr, \tag{3.18}$$

can be computed numerically, from which,

$$A_e^*(z) = \frac{\int_0^{r_0} A_d(r, z)2\pi r dr}{A_d}. \tag{3.19}$$

Electrode Position	z	A_e^*
Closer edge of electrode	24 cm	1.1 cm^2
Closer gas inlet	33 cm	2.0 cm^2
Middle of electrodes	37 cm	2.6 cm^2
Further gas inlet	41 cm	3.1 cm^2
Further electrode edge	49 cm	4.5 cm^2

Table 3.2: The effective viewing area of a collimated vacuum photodiode computed at various points on the plasma electrodes.

Let us compute the effective area A_e^* at the midpoint of the electrodes. At the midpoint of the electrodes, $z = D + L/2$, and $A_e^* = 5.0$ cm^2. This area corresponds to a circle of radius $r^* = \sqrt{A_e^*/\pi} = 1.3$ cm. Note that this effective radius is significantly smaller than $\rho_0 = 4.7$ cm, the radius of the field of view, but larger than $R = 0.38$ cm, the radius of the collimator. In fact, r^* is closer to the geometric mean: $\sqrt{R\rho_0} = 1.3$ cm.

Because of the gapped magnets in front of the collimator, the above calculation of A_e^* is too large because the magnets will further shadow the detector. The geometric consideration of incorporating the magnets into the above calculations are considerable. Instead, we note that the magnets occupy about half of the collimator area and estimate A_e^* to be about half its value computed above: $A_e^* = 2.57$ cm^2. The effective areas at other distances from the array are shown in Table 3.2.

3.6 Final Product

The final version of the array contains twelve fully functional channels arranged in a T-shape to measure both vertical and horizontal variations. In summary,

- Aluminum disks with a light sanding serve as photoemitting cathodes, providing large signals that do not require amplification.
- A bias voltage is needed to overcome space-charge limitations.
- The detector must be carefully shielded both by using an enclosure and by careful layout of the anode and cathode to protect against capacitive coupling.
- Ground loops are prevented by not electrically connecting detector ground to the chamber ground. However, RF ground loops are still present, and these ground currents have been diverted from the cables by the combined use of ferrites and shunts.
- The use of semi-rigid coaxial cables reduces noise and provides a means of taking the detector signals out of the vacuum chamber.
- Magnets placed on the collimators deflect incoming charged particles. If energetic ions manage to pass the magnet, they can induce both positive and negative spurious signals, in part due

to a transient voltage that appears inside the enclosure during a shot.

- Each detector is collimated so that it views an individual area of the plasma. The effective area seen by the detector is less than its full field of view but larger than the collimator cross-sectional area and is estimated at 2.6 cm^2.

Thus, the difficulties encountered in implementing vacuum photodiodes on the Caltech Solar Loop Experiment have been resolved, and it would be straightforward to build and install more of these detectors on either the Solar Loop or Spheromak Experiments. The true utility of this diagnostic, however, is the subject of the next chapter.

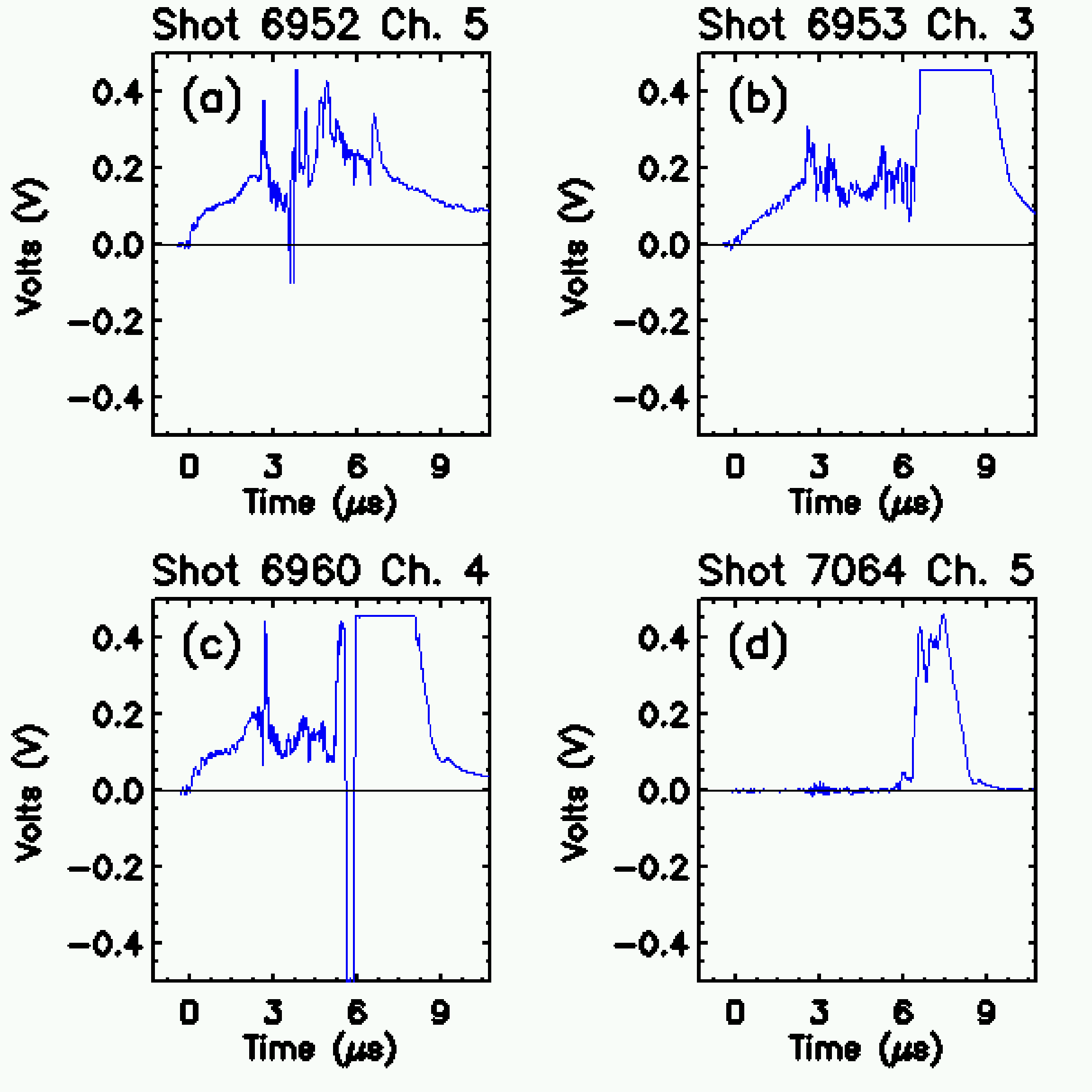

Figure 3.14: A collection of vacuum photodiode data with spurious signals due to charged particles: (a) a shot with negative spikes (b) a shot with a large positive signal late into the plasma lifetime (c) a shot with a negative dip preceding a positive peak (d) a shot with a late positive peak obtained with no bias voltage.

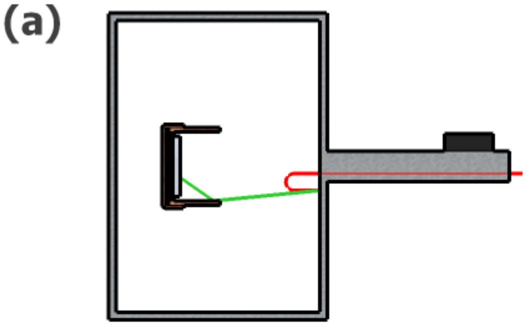

Figure 3.15: The transient voltage between the vacuum photodiode and the enclosure is responsible for positive and negative spurious signals. In this figure, energetic ions that pass the magnet are shown in red, whereas secondary electrons are shown in green. (a) When the transient voltage is positive, secondary electrons produced by the incoming ions are accelerated towards the anode, where they generate more secondaries that strike the cathode. This produces the negative spurious signals. (b) When the transient voltage is negative, the ions themselves are attracted to the detector and induce the late positive spurious signals. They might strike the cathode directly or bounce off the anode first.

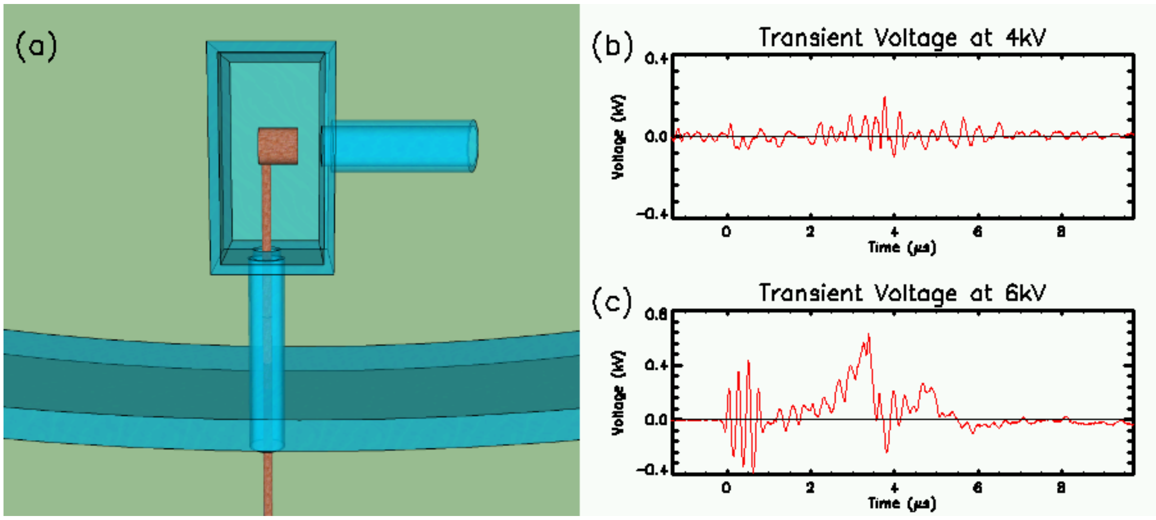

Figure 3.16: (a) There are two "grounds" on the detector: the detector ground shown in red, and the chamber ground shown in blue. The two grounds are ultimately connected through a long path, but the distance is large enough that the two grounds can be at different potentials. (b) The voltage between these two "grounds," as measured with a high-voltage probe, for a 4 kV counter-helicity discharge (c) The same measurement for a 6 kV discharge.

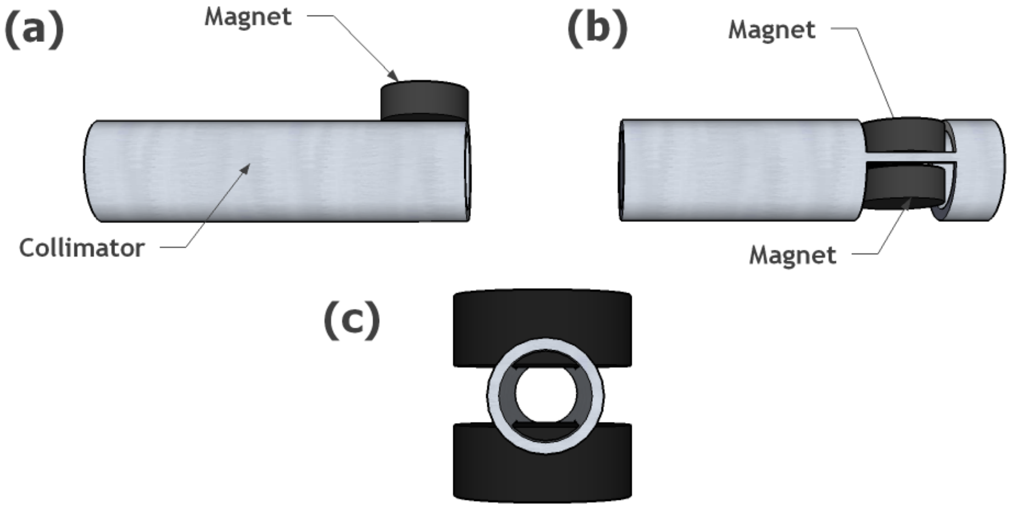

Figure 3.17: (a) The original collimator had a single magnet. (b) The upgraded collimator uses two magnets placed in notches. (c) The gap region has a uniformly high field strength.

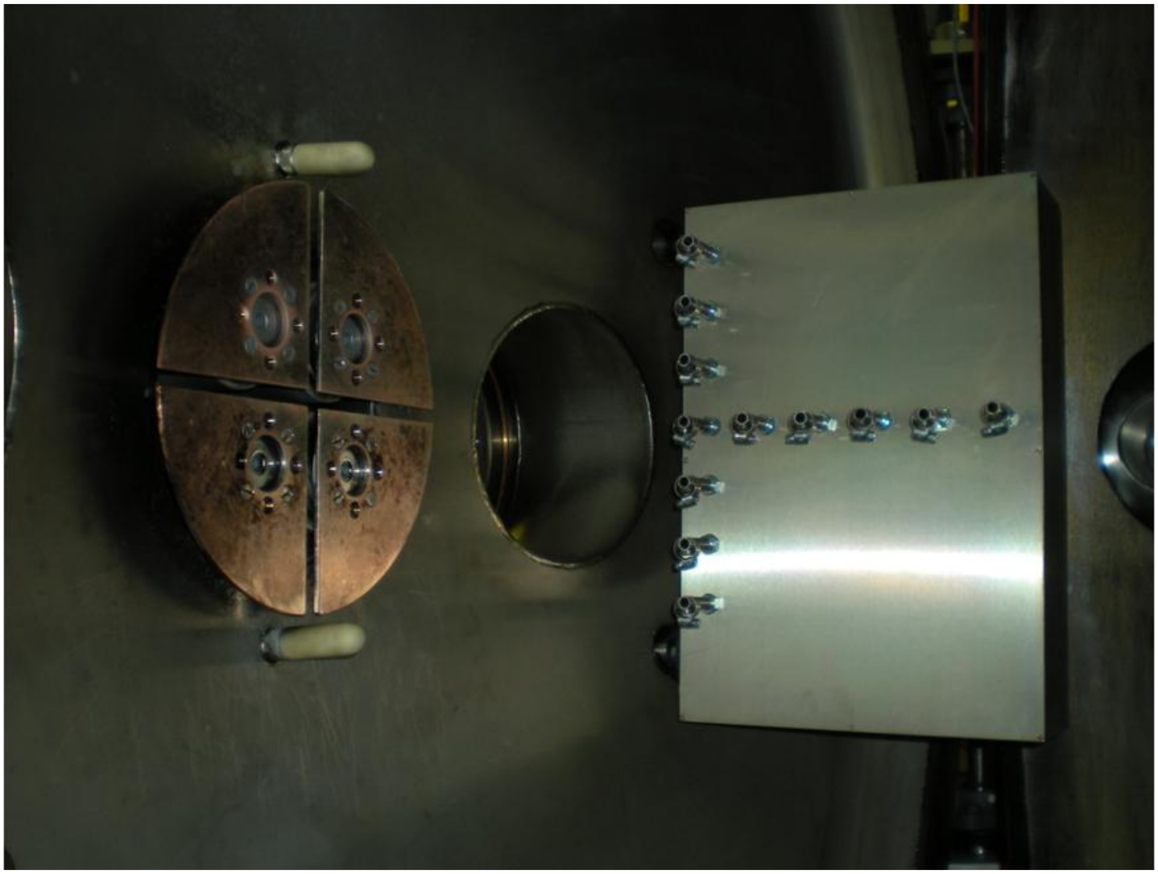

Figure 3.18: The array consists of twelve active channels, seven vertical and six horizontal, and looks across the electrodes.

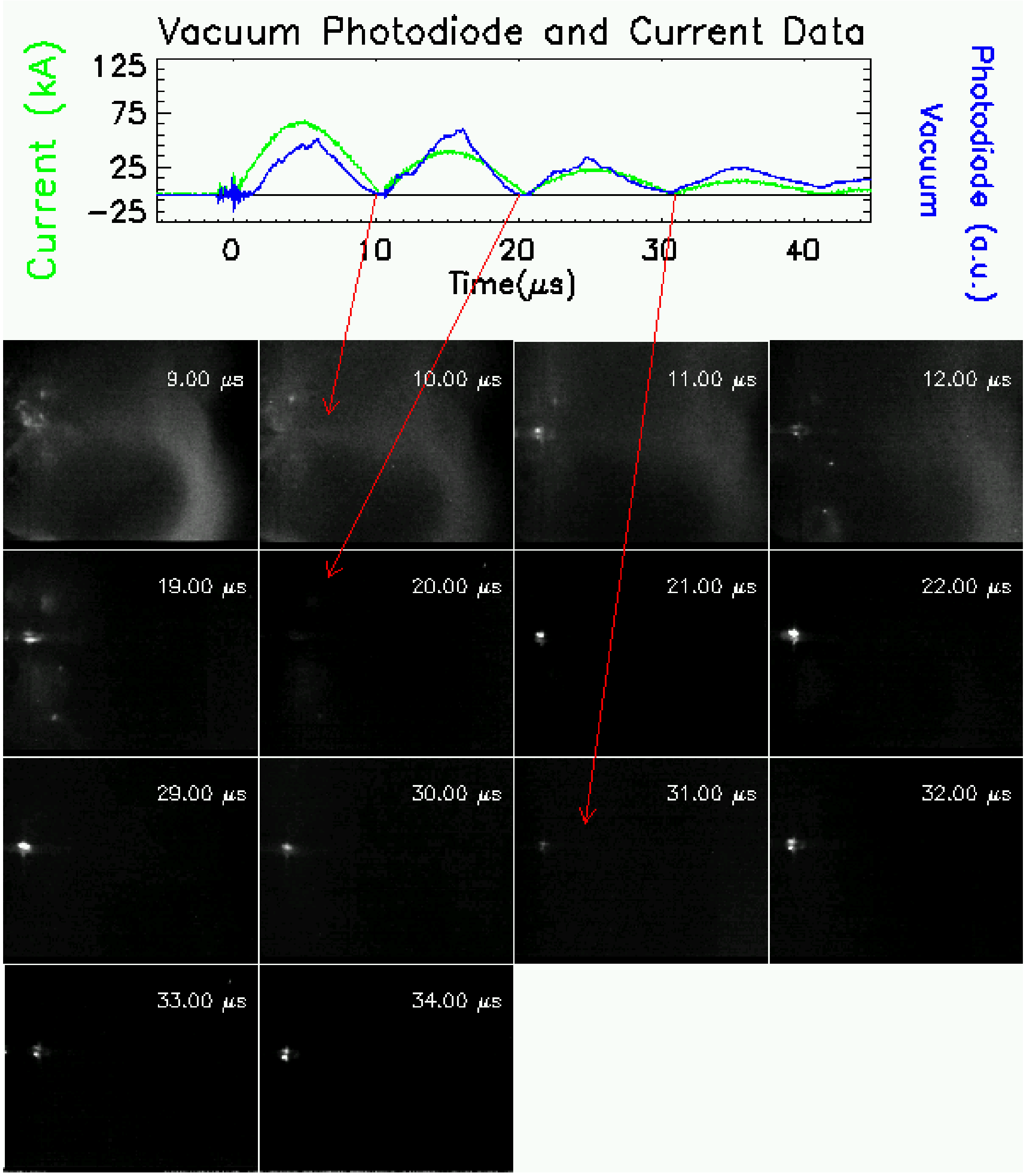

Figure 3.19: Vacuum photodiodes can detect radiation emitted by electrode arcing, which obscures the desired photosignal from the plasma. The vacuum photodiode data, plotted in blue, is overlayed with the absolute value of the current trace, plotted in green. The vacuum photodiode signal looks like a rectified version of the current trace, and the minima of the photodiode signal coincide with the zeros of the current. This plot extends to 45 μs, while the plasma only lasts until $\sim$ 12 μs. Thus, the data after $\sim$ 12 μs is not from the plasma itself. In the Imacon image, the frames have been timed to take pictures very late into the shot in order to observe what is happening at the electrodes after the plasma. Localized arcing is observed between the electrodes. The arcing abates at the minima of the vacuum photodiode signal, implying that the late signal is due to the arcing.

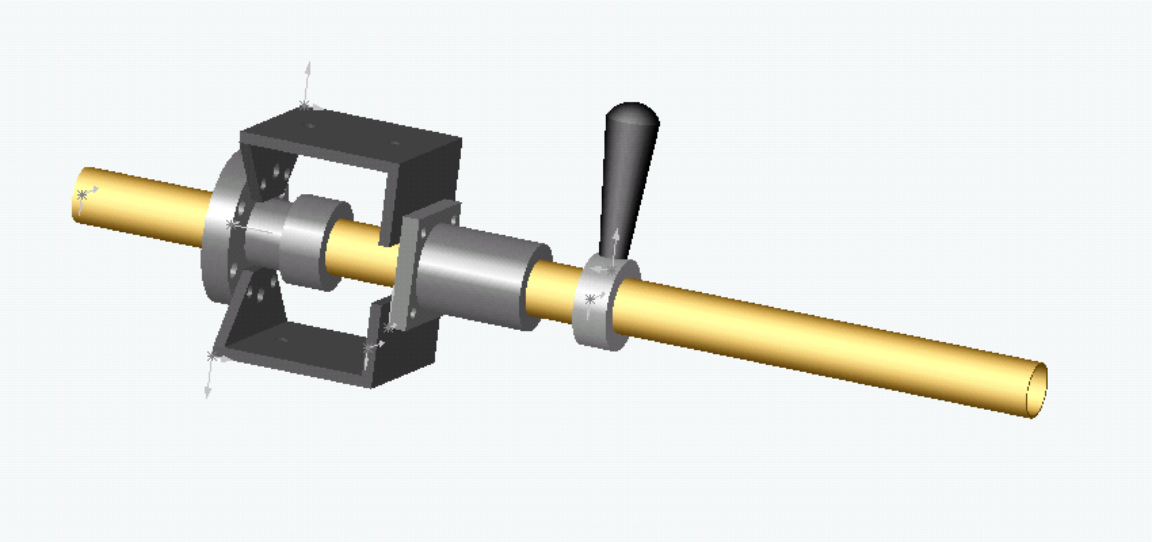

Figure 3.20: A support system is needed to handle the torque of the array. The long tube is the 1" stainless steel support arm of the array. Starting from the left of the figure, the first component is a quick-disconnect flange that mates with a 2 1/4" port on the chamber. After that are two aluminum brackets followed by an aluminum linear bearing. The linear bearing prevents bending of the support arm against the torque of the array. The aluminum brackets hold the bearing in place. Finally, a collar and fluted handle provide a grip for rotating the array.

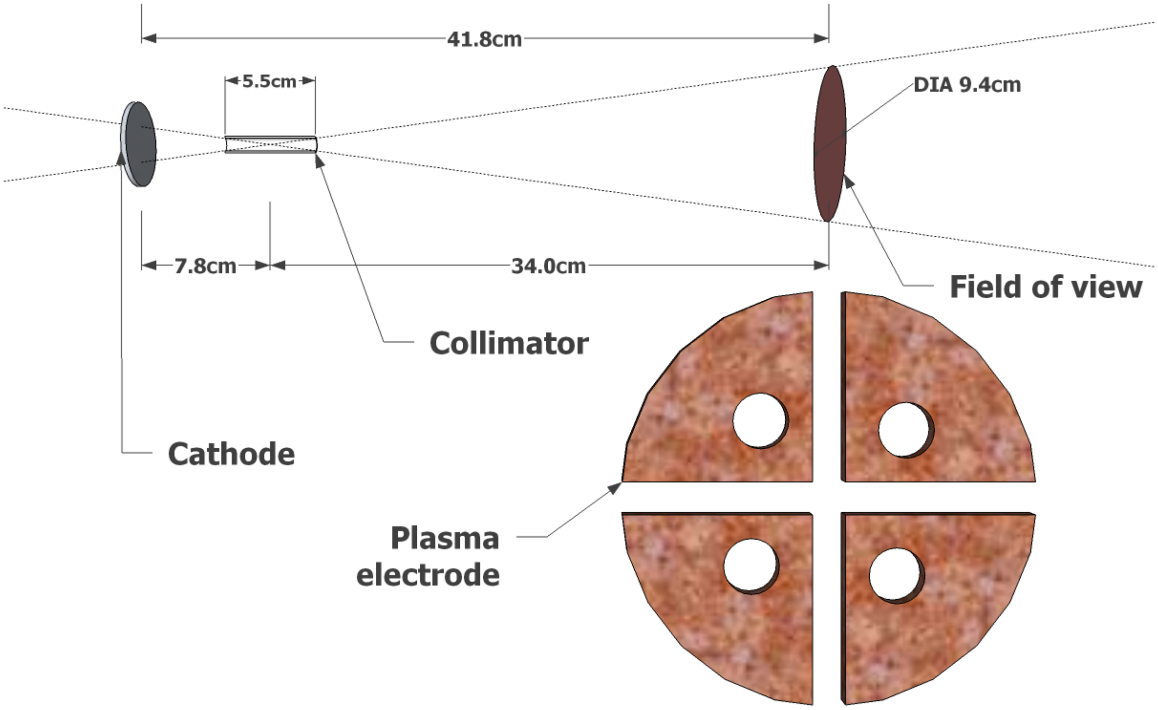

Figure 3.21: Given the collimator dimensions, the detector's view cone, depicted by the dashed lines, can be determined. At the center of the electrodes, the view cone has a diameter of 9.4 cm.

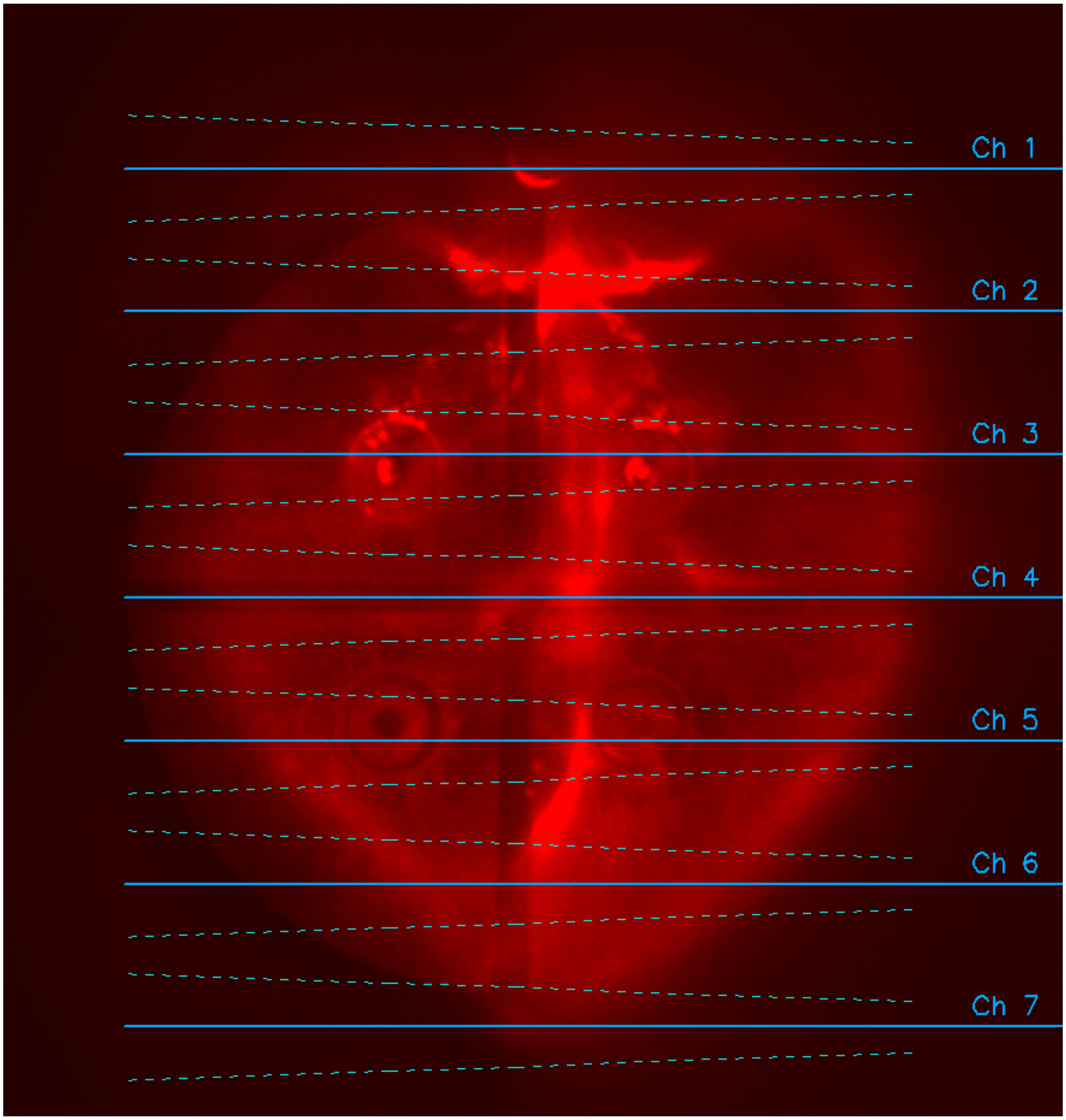

Figure 3.22: This is a head-on photograph of the electrodes in the middle of a shot. The lines superimposed over the image represent the fields of view of the vacuum photodiodes. The thick horizontal line is the central axis of each detector. The dashed lines denote the radius of the effective area of each detector, as computed in Sec. 3.5.3. This radius does not account for the additional shadowing by the magnets.

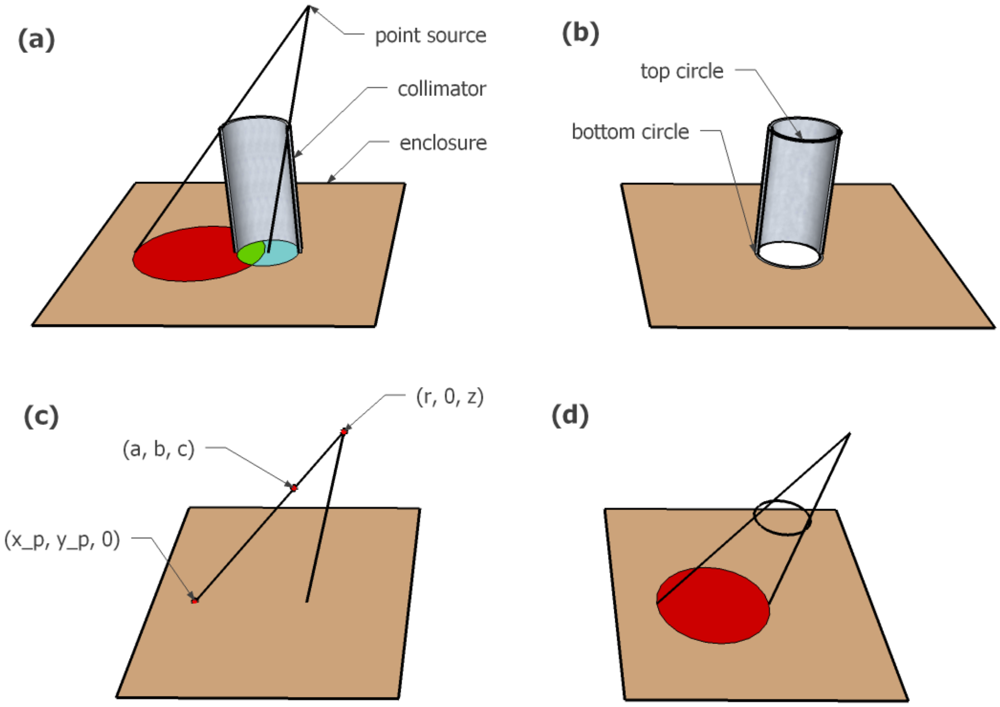

Figure 3.23: (a) The collimator, shown here in a cutaway view, casts a shadow over the entrance to the detector. The illuminated area is drawn in green, whereas the shadow is drawn in blue and red. (b) The top and bottom circles are defined here for clarity. (c) Projection of a point (a, b, c) onto the $z = 0$ plane given a point source at $(r, 0, z)$. The projection point is labeled $(x_p, y_p, 0)$. (d) The projection of a circle is another circle with a shifted center and larger radius.